IRAQI JOURNAL OF APPLIED PHYSICS LETTERS

Iraqi Journal of Applied Physics Letters (IJAPLett) is a scientific periodical sponsored and published by the Iraqi Society for Alternative and Renewable Energy Sources and Techniques (I.S.A.R.E.S.T.). The Editorial Board is responsible for the scientific content and other editorial matters relating to the Journal. Manuscripts submitted are first screened by the editors; those on subject matters within the scope of the IJAPLett are sent to an expert referee for evaluation and may be sent to a second reviewer if necessary. This screening process helps to assure an appropriate focus as well as high scientific quality of the Journal. The IJAPLett welcomes submission of papers and letters in applied physics and related fields of science, engineering and technology. They should have something in common with what we now publish on inanimate materials and processes therein: structures, transport, physical, electrical, dielectric, magnetic, and optical properties. Our basic criterion stated below will continue to apply: papers must contain science, especially physics, and there must be an application. We advise authors submitting papers to suggest the names of at least two possible reviewers, with full information on addresses, phone and email. Suggestions of reviewers are welcome regardless of the subject.

EDITORIAL BOARD

Dayah N. RAOUF
Professor, Editor-in-Chief
School of Applied Sciences, University of Technology, IRAQ
dayah@ijap.org

Walid K. HAMOUDI
Professor, Member
School of Applied Sciences, University of Technology, IRAQ
walid@ijap.org

Raid A. ISMAIL
Professor, Member
School of Applied Sciences, University of Technology, IRAQ
raid@ijap.org

Raad A. KHAMIS
Professor, Member
School of Applied Sciences, University of Technology, IRAQ
raad@ijap.org

Oday A. HAMADI
Managing Editor
Department of Biology, Faculty of Education,
The Iraqi University, Baghdad, IRAQ
oday@ijap.org

Rania A. MARKUB
Middle East Coordinator
School of Applied Sciences, University of Technology, IRAQ
rania@ijap.org

Haitham M. MIKHLIF
Reviews Editor
Department of Physics, Al-Mustansiriya University, IRAQ
haitham@ijap.org

Intesar F. RAMLEY
Industrial Relation Coordinator
INToo Software, Vancouver, V4B 4W4, BC, Canada
intesar@ramley.com

Editorial Office
P. O. Box 55259, Baghdad 12001, IRAQ
Website: www.ijap.org
Email: editor@ijap.org
Mob.: 00964 7702523071

ADVISORY BOARD

Abdullah M. SUHAIL, Assistant Professor, Department of Physics, College of Science, University of Baghdad, IRAQ
Andrei KASIMOV, Professor, Institute of Material Science, National Academy of Science, UKRAINE
Ashok KUMAR, Professor, Harcourt Butler Technological Institute, Kanpur-208 002, INDIA
Chang Hee NAM, Professor, Korean Advanced Institute of Science and Technology, Taejon, KOREA
El-Sayed M. FARAG, Professor, Department of Sciences, College of Engineering, Al-Minofiya University, EGYPT
Franko KUEPPERS, Assistant Professor, College of Optical Sciences, University of Arizona, Tucson, U.S.A
Heidi ABRAHAMSE, Professor, Faculty of Health Sciences, University of Johannesburg, SOUTH AFRICA
Kais A. AL-NAIMEE, Assistant Professor, National Institute of Applied Optics, University of Florence, Florence, Italy
Khaled A. AHMED, Assistant Professor, Department of Physics, College of Science, Al-Mustansiriya University, IRAQ
Manal J. AL-KINDY, Assistant Professor, Department of Electronic Engineering, Al-Nahrain University, IRAQ
Mansoor SHEIK-BAHAE, Associate Professor, Dept. of Physics and Astronomy, University of New Mexico, U.S.A
Marc BURGELMAN, Professor, Electronics and Information Systems, University of Gent, Gent, BELGIUM
Mazin M. ELIAS, Professor, Laser Institute for Postgraduates, University of Baghdad, Baghdad, IRAQ
Mohammed A. HABEEB, Professor, Department of Physics, Faculty of Science, Al-Nahrain University, IRAQ
Muhammad A. HUSSAIN, Assistant Professor, Dept. of Laser and Optoelectronics Eng., Al-Nahrain University, IRAQ
Mutaz S. ABDUL-WAHAB, Assistant Professor, Electric and Electronic Eng., University of Technology, IRAQ
Shivaji H. PAWAR, Professor, D. Y. Patil University, Kasaba Bawada, Kolhapur-416 006, INDIA
Xueming LIU, Professor, Department of Electronic Engineering, Tsinghua University, Beijing, CHINA
Yanko SAROV, Assistant Professor, Central Lab. Of Optics, Bulgarian Academy of Science, Sofia, BULGARIA
Yushihiro TAGUCHI, Professor, Department of Physics, Chuo University, Bunkyo-ku, Tokyo, JAPAN

SPONSORED AND PUBLISHED BY

THE IRAQI SOCIETY FOR ALTERNATIVE AND RENEWABLE ENERGY SOURCES AND TECHNIQUES (I.S.A.R.E.S.T.)

ISSN 1999-656X © ALL RIGHTS RESERVED PRINTED IN IRAQ

“ INSTRUCTIONS TO AUTHORS “

CONTRIBUTIONS

Contributions to be published in this journal should be original research works, i.e., those not already published or submitted for publication elsewhere, individual papers or letters to editor.

SUBMISSION OF MANUSCRIPTS

Manuscripts should be submitted to the editor at the mailing address:

Iraqi Journal of Applied Physics Letters
Editorial Board, P. O. Box 55259, Baghdad 12001, IRAQ
ijaplett@ijap.org , editor@ijap.org

MANUSCRIPTS

Two hard copies with soft copy on a compact disc (CD) should be submitted to Editor in the following configuration:

- Double-spaced one-side A4 size with 2.5 cm margins of all sides
- Times New Roman font (16pt bold for title, 14pt bold for names, 12pt bold for headings, 12pt regular for text)
- Letters should not exceed 10 pages.
- Manuscripts presented in English only are accepted.
- English abstract not exceed 150 words
- 4 keywords (at least) should be maintained on (PACS preferred)
- Author(s) should express all quantities in SI units
- Equations should be written in equation form (*italic* and symbolic)
- Figures and Tables should be separated from text
- Figures and diagrams can be submitted in colors for assessment and they will be returned to authors after provide printable copies
- Charts should be indicated by the software used for
- Only original or high-resolution scanner photos are accepted
- For electronic submission, articles should be formatted with MS-Word software.

AUTHOR NAMES AND AFFILIATIONS

It is IJAPLett policy that all those who have participated significantly in the technical aspects of a paper be recognized as co-authors or cited in the acknowledgments. In the case of a paper with more than one author, correspondence concerning the paper will be sent to the first author unless staff is advised otherwise.

Author name should consist of first name, middle initial, last name. The author affiliation should consist of the following, as applicable, in the order noted:
- Company or college (with department name or company division)
- Postal address, city, state, zip code, country, telephone, and e-mail

REFERENCES

The references should be brought at the end of the article, and numbered in the order of their appearance in the paper. The reference list should be cited in accordance with the following examples:

[1] X. Ning and M.R. Lovell, "On the Sliding Friction Characteristics of Unidirectional Continuous FRP Composites", *ASME J. Tribol.*, 124(1) (2002) 5-13.

[2] M. Barnes, "Stresses in Solenoids", *J. Appl. Phys.*, 48(5) (2001) 2000–2008.

[3] J. Jones, "Contact Mechanics", Cambridge University Press (Cambridge, UK) (2000), Ch.6, p.56.

[4] Y. Lee, S.A. Korpela and R. Horne, "Structure of Multi-Cellular Natural Convection in a Tall Vertical Annulus", Proc. 7th International Heat Transfer Conference, U. Grigul et al., eds., Hemisphere (Washington DC), 2 (1982) 221–226.

[5] M. Hashish, "Waterjet Technology Development", High Pressure Technology, PVP-Vol. 406 (2000), 135-140.

[6] D.W. Watson, "Thermodynamic Analysis", ASME Paper No. 97-GT-288 (1997).

[7] C.Y. Tung, "Evaporative Heat Transfer in the Contact Line of a Mixture", Ph.D. thesis, Rensselaer Polytechnic Institute, Troy, NY (1982).

PROOFS

Authors will receive proofs of papers and are requested to return one corrected hard copy with a WORD copy on a compact disc (CD). New materials inserted in the original text without Editor permission may cause rejection of paper.

COPYRIGHT FORM

Author(s) will be asked to transfer copyrights of the article to the Journal soon after acceptance of it. This will ensure the widest possible dissemination of information.

OFFPRINTS

Authors will receive offprints free of charge and any additional offprints can be ordered.

SUBSCRIPTION AND ORDERS

Annual fees (4 issues per year) of subscription are:

- 50 US$ for individuals inside Iraq.
- 100 US$ for establishments inside Iraq.
- 100 US$ for individuals abroad.
- 200 US$ for establishments abroad.

Fees are reduced by 25% for I.S.A.R.E.S.T. members. Orders of issues can be submitted by contacting the editor-in-chief or editorial office at **subscription@ijap.org** to maintain the address of issue delivery and payment way.

Linear Adaptive Antenna Array Geometry Effects on Radiation Pattern

Adheed H. Sallomi [1]
Haitham H. Mikhlif [2]
Sana R. Salim [2]

[1]*Department of Electrical Engineering, College of Engineering, Al-Mustansiriyah University, Baghdad, Iraq*
[2]*Department of Physics, College of Sciences, Al-Mustansiriyah University, Baghdad, Iraq*

Over the last few years, the number of subscribers to wireless services has increased at an explosive rate. Smart-antenna technology compared to conventional antenna has the ability to increase the number of simultaneous users, and satisfy the requirements of spectral efficiency, and coverage in wireless communication systems. In this paper the radiation pattern and performance of linear smart antenna array is investigated by considering multiple directions of arrivals of signals. The simulations done confirmed that smart antenna systems using Least Mean Square (LMS) algorithm are able to adjust their pattern to enhance desired signals, and reduce interference. The results also show that smart antenna radiation patterns are related to the number of elements in the array, the inter-element spacing, and amplitude distribution.

Keywords: Wireless technology, Radioactive waves, Communication engineering, Smart antenna
Received: 01 January 2010, **Revised**: 17 March 2010, **Accepted**: 24 March 2010

1. Introduction

Omni-directional or sectored antennas used in current wireless communication systems, can be considered as an inefficient use of power as most of it has been radiated in other directions than toward the user. Signals that miss the intended user will cause interference to other users in the same or adjoining cells [1].

The concept of smart antennas is to employ base station antenna patterns that are not fixed in any direction but adapt to the current radio conditions. In other words, the antenna is to direct a single beam to each user. Smart antennas direct their main lobe, with increased gain, in the direction of the user, and they direct nulls in directions away from the main lobe [2-3]. Smart antennas shown in Fig. (1) consist of an array of antenna elements and a smart processing of antenna signals.

In this paper, we will concentrate on the adaptive arrays that make use of the Direction of Arrival (DOA) information from the desired user to steer the main beam towards the desired user. The signals received by each antenna element are weighted and combined to create a beam in the direction of the mobile by utilizing signal-processing algorithms [4]. These algorithms determine the uplink weight vectors for performing beam-forming on the received signals as well as the downlink weight vectors for performing beam forming on the transmitted signals [3].

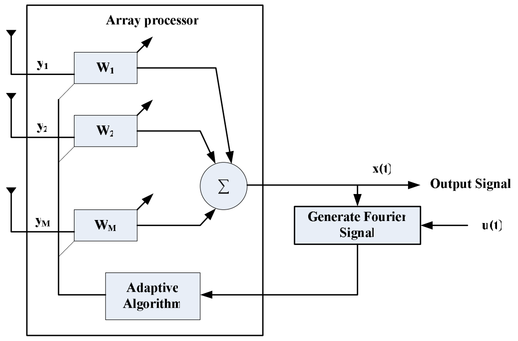

Fig. (1) Smart Antenna Construction

2. Smart Antenna Operation Theory

The signals collected by the antenna elements are down converted, sampled and digitized to generate the beam former inputs (x_1, x_2… x_M). These signals contain both the desired signal and the interfering signals and these are appropriately multiplied by complex weight vectors (w_1, w_2… w_M) and combined to generate the array output $y(t)$ as [1]:

$$y(t) = w^H(t).x(t) \quad (1)$$

where w^H denotes the transposition of the complex conjugated vector

The array output is then compared with some reference signal $u(t)$ to generate an error signal, which is then adaptively minimized by an adaptive algorithm. The error signal, which is used to control the weights, is given as:

$$e(t) = u(t) - w^H(t).x(t) \quad (2)$$

The weights are adjusted according to some minimization criteria such that the Mean Squared Error (MSE) between the array output and the reference signal is minimized, where the squared error is expressed as:

$$e^2(t) = [u(t) - w^H(t).\, x(t)]^2$$

$$e^2(t) = [(u(t))^2 - 2\, w^H(t).x(t)\, u^*(t) + w^H w x(t) x^H(t)] \quad (3)$$

One of the various algorithms that are based on the MSE criteria is the Least Mean Square (LMS) algorithm. It is widely used to synthesis multi-beams patterns in the directions of the different users by weights control due to its low computational complexity, good stability and robustness against errors [1,5].

The weight starts with certain initial value $w(t)$, and then updated at time (t+1), that is given by[5]:

$$w(t+1) = w(t) - \mu.\nabla_w.E(e^2(t)) \quad (4)$$

where (t+1) denotes the new weights at the (t+1)th, μ is the positive step size that controls the convergence rate which determines how close the estimated weights approach to the optimal weights, and $\nabla_w.E(e^2(t))$ is an estimate of the gradient of the MSE. In most cases, the weight vector is updated during some training sequence due to the faster convergence rate.

The summaries of the LMS algorithm are [6]:

Array Output:

$$y(t) = w^H(t).x(t)$$

Estimation error:

$$e(t) = u(t) - y(t) = u(t) - w^H(t).x(t)$$

Weight adaptation:

$$w(t+1) = w(t) + \mu.x(t).e^*(t)$$

There are basic factors which influence the performance of linear antenna array and contribute to the shaping of the overall pattern of the array with identical omnidirectional elements. An array factor, in general, is a function of the number of elements, the inter-element spacing, and the geometrical configuration of the elements in the array (linear, circular, rectangular, etc) [7].

For an array of identical elements, by principle of pattern multiplication, the overall radiation pattern is found as the product of the individual element radiation pattern with its array factor [8].

3. Simulation of Smart Antenna Array Parameters

To study the effect of number of antenna elements and the inter-spacing element on the pattern shaping, we consider a linear array of N equi-spaced isotropic antenna elements positioned along the x-axis.

One training sequence of 500 input signals signed with values of 1 or –1 is used to simulate a transmitter sending binary values.

The carrier frequency (f_c) of transmitted training sequences is set to 900MHz, which means that the value of the wavelength (λ) is set to 0.33m. For simulations of one transmitted signal with two paths (u1 and u2), the first path was assumed to arrive at the base station at an angle of 30° with a gain amplitude of 0.5dB and the second path is assumed to arrive at an angle of -45° with a gain amplitude of 0.8dB. The propagation delay (Tu1) from transmission to reaching the first antenna element was set to 100μs for the first path, however, the second multipath component of the signal is set to arrive at the antenna array one sample period behind the first multipath. The step-size parameter μ for the LMS algorithm is set to 0.008.

Figure (2) illustrates the scenario of the simulated case. The radiation patterns are presented in both linear and polar plots. The MATLAB program is used as a program to simulate the linear array smart antenna parameters.

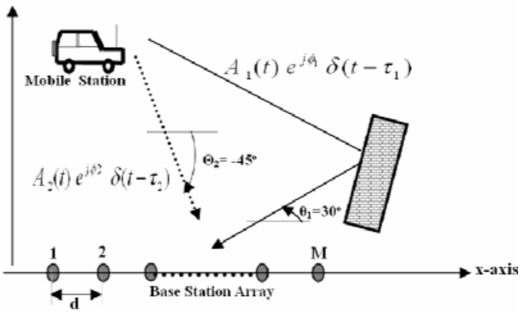

Fig. (2) Test Case Scenario (One signal with Two Paths)

3-1 Effect of Varying Number of Elements

For this simulation the inter-element spacing is set to be $\lambda/2$, where λ is the wave length. Figure (3) illustrates the polar and linear radiation pattern for 4, 8, 16 and 32 elements linear arrays.

Simulations results obtained have proved that an increase in the number of elements in a linear array would result in higher directivity, as well as a sharper and narrower beam width, but this brings about more side-lobes. Results also prove that the ripple rate would be higher if there was an increase in the number of elements in the linear array. It has been shown that the interference rejection capability of the array improves as the number of antenna elements increases. Therefore, the number of elements in an array is most useful for shaping main beam of an antenna pattern as the side lobe level is at a satisfactory level.

3-2 Effect of Varying Inter-elements Spacing

Figure (4) illustrates the polar radiation pattern for an 8-elements linear array for an inter-element spacing (*d*) of quarter wavelength ($\lambda/4$), half wavelength ($\lambda/2$), ($3\lambda/4$), full wavelength (λ), double wavelength (2λ) and triple wavelength (3λ).

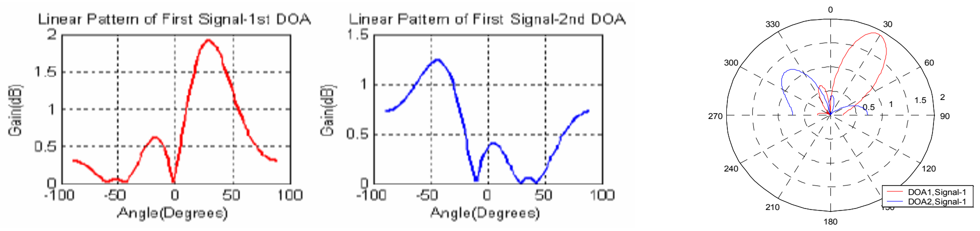

4-Element Linear Array **4-Element Linear Array**

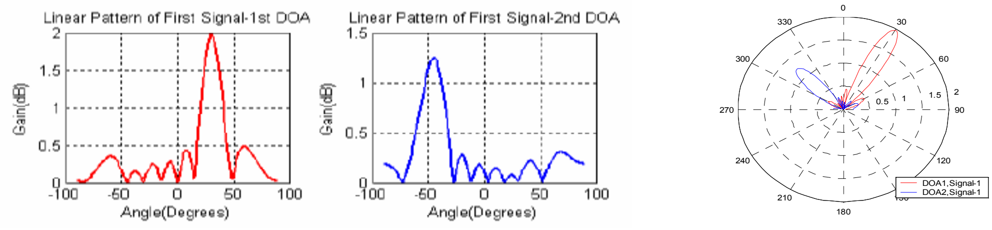

8-Element Linear Array **8-Element Linear Array**

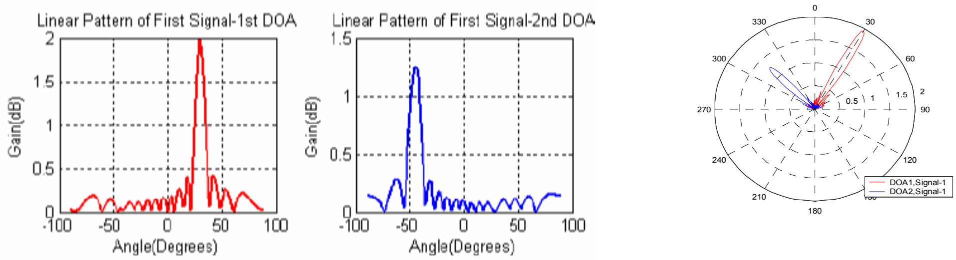

16-Element Linear Array **16-Element Linear Array**

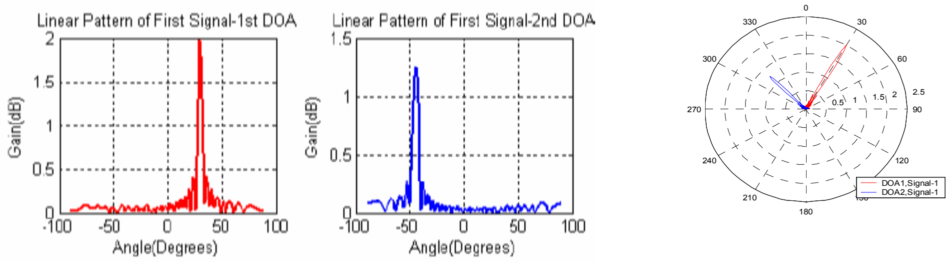

32-Element Linear Array **32-Element Linear Array**

Fig. (3) Polar and Linear Antenna Pattern with Different Number of Elements

It is observed that an increase in inter-element spacing in a linear array will result in higher directivity and a smaller beamwidth. Although this is a favorable condition, it is found that, the number of undesirable side lobes also increases with increasing inter-element spacing.

From Fig. (4), it can be noticed that interference rejection ability of the array is quite poor when the antenna elements are very tightly spaced ($d<0.5\lambda$). This is because in such a situation, the directivity of the array is reduced and the closely spaced array approximates an omnidirectional antenna. As the array elements are moved apart, the interference rejection capability increases. It can be noticed that by increasing array length, linear array has the ability to reduce interference.

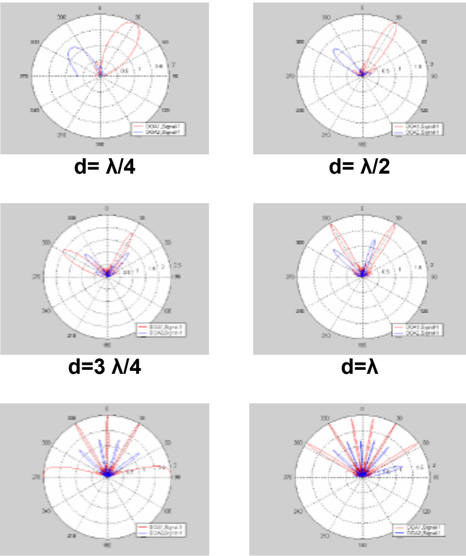

d= λ/4 d= λ/2

d=3 λ/4 d=λ

d=2λ d=3λ

Fig. (4) 8-Elements Antenna Pattern for Different Inter-Spacing

From the results of the simulations, it is seen that radiation patterns are related to the number of elements in the array, the inter-element spacing. Thus, there is always a compromise between the influencing parameters.

It is also proven that in a linear equally spaced array, grating lobes can appear in the antenna pattern if the elements are spaced more than ($\lambda/2$). For an antenna array oriented along the x-axis with every array lobe that the array forms, another lobe may appear. These grating lobes are additional major lobes that have intensity equal to that of the main lobe. For the separation range ($0.4\lambda<d<0.5\lambda$), the grating lobes disappear and a narrow beam can be formed on the reference user leading to good performance of the receiving system involving the array.

It can be noticed that the number of multipath has a significant effect on the performance of the smart antenna system.

4. Conclusion

The overall pattern, which is formed by combining the radiation pattern of a single omnidirectional antenna and the array factor of the linear smart antenna array, is analyzed. Simulations results show that smart antenna radiation pattern is related to the number of elements in the array, the inter-element spacing, and amplitude distribution. Thus, there is always a compromise between those parameters. Results obtained proved that an increase in the number of elements and inter-element spacing in a linear array would result in higher directivity and a smaller beamwidth. It was found that the amplitude of the gain had the most effect on the system, with the phase having little to no effect. Lastly, simulation results proved that the Least Mean Square (LMS) algorithm has the capability to steer the multiple main beams in the directions of the different paths but in the same cell which denote that smart antenna systems are able to reuse intra-cell frequency.

References

[1] A.H. Sallomi, "Smart Antenna Performance Analysis for Mobile Communications in Urban Environments", Ph.D. thesis, University of Technology, Baghdad (2007).

[2] M.C. Wells, *IEE Proc. on Commun.*, 143(5) (1996) 304-310.

[3] M. Mouhamadou and P. Vaudon, *Prog. in Electromag. Res.*, PIER60 (2006) 95–106.

[4] H. Liu and G. Xu, *IEEE Trans. on Commun.*, 45(2) (1997) 187-199.

[5] H. Steyskal, *IEEE Trans. on Antennas and Propagation*, 31 (1983) 163-166.

[6] M. Chryssomallis, *IEEE Antennas and Propagation Magazine*, 42(3) (2000) 129-136.

[7] K.G. Vijay and D. Wang, *IEEE Antennas and Wireless Propagation Letters*, 3(1) (2004) 66-70.

[8] J.H. Winters, *IEEE Personal Commun.*, 5(1) (1998) 23-27.

Synchronization Scheme for Secured Communications System Based on Chaotic Signals

Paul E. Sterian

Research Center of Optical Engineering and Photonics, Politehnica University of Bucharest, Bucharest, Romania

---

In this work, a numerical investigation of a synchronization scheme for secure communication implemented with nonlinear optical ring cavities is performed. We have demonstrated that masking the information in a chaotic optical wave from a nonlinear ring cavity is technically feasible in a secured communication system. The synchronization is robust and analog information transmission is suitable for the specific case considered.

Keywords: deterministic chaotic system; synchronization; communication system
Received: 20 November 2009, **Revised**: 29 January 2010, **Accepted**: 5 February 2010

1. Introduction

Synchronization of periodic signals is a common phenomenon in many scientific areas. On the other hand, deterministic chaotic systems present the property of sensitivity with respect to initial conditions: two identical autonomous chaotic systems starting at very close initial conditions evolve so that the trajectories in the phase space start diverging exponentially and for large times they are uncorrelated. It seems that synchronization can not be reached in such systems. Nevertheless, it was recently proven [1] that certain chaotic systems may be linked such that their chaotic motions synchronize. The research in this direction is greatly motivated by the possibility of using chaotic signals as broadband carriers of analog and digital information [2-6]. Tests were performed using electronic circuits. For example, the message was added to a chaotic carrier signal and transmitted to a system which is a copy of that one creating the chaotic signal. The receiver synchronizes with the carrier signal and the message is recovered by a simple substraction of the receiver signal from the total transmitted one in an adequate electronic block.

It was a widespread idea that deterministic chaos will not have practical applications. The ability to design synchronizing chaotic systems may open opportunities for the use of chaotic signals in private communication, taking advantage of the unique features of chaotic signals. More than that, synchronization is structurally stable in this case and using chaotic signals may be preferable to periodic signals in certain cases where robustness is important.

2. Pecora-Caroll Synchronization Scheme

This is the most known method for synchronization subsystems [1]. An autonomous n-dimensional dynamical system given in the form of a flow:

$$\dot{\mathbf{u}} = \mathbf{f}(\mathbf{u}) \qquad (1)$$

is decomposed into two subsystems,

$$\dot{\mathbf{v}} = \mathbf{f}_{\mathrm{v}}(\mathbf{v}, \mathbf{w}) \qquad (2a)$$

$$\dot{\mathbf{w}} = \mathbf{f}_{\mathrm{w}}(\mathbf{v}, \mathbf{w}) \qquad (2b)$$

with $\mathbf{v} = (u_1, ..., u_m)$, $\mathbf{w} = (u_{m+1}, ..., u_n)$ and $\mathbf{f} = (\mathbf{f}_{\mathrm{v}}, \mathbf{f}_{\mathrm{w}})$

Now create a new $\mathbf{w}'$ subsystem driven by the $\mathbf{v}$ subsystem:

$$\dot{\mathbf{w}}' = \mathbf{f}_{\mathrm{w}}(\mathbf{v}, \mathbf{w}') \qquad (3)$$

i.e., given by the same vector field $\mathbf{f}_{\mathrm{w}}$. Subsystem $\mathbf{w}'$ synchronizes with subsystem $\mathbf{w}$, i.e.,

$\|\mathbf{w}-\mathbf{w}'\| \to 0$ as $t \to \infty$

if the conditional Lyapunov exponents of subsystem $\mathbf{w}$ are all negative [1].

3. Proposed Communication System

A communication scheme compatible with the above synchronization method is presented in Fig. (1). In the transmission area, the subsystem $\mathbf{u}$ is called *master* system, while the $\mathbf{w}$ and $\mathbf{w}'$ subsystems are referred to as *slave* systems. Here, the link between the two subsystems in the transmission area is unidirectional. The encryption is done by using the chaotic signal of the slave system at the transmitter as carrier for the message. At the receiver, the slave system synchronizes with its replica at the transmitter through the one linking drive signal. This allows the extraction of the information from the total transmitted signal.

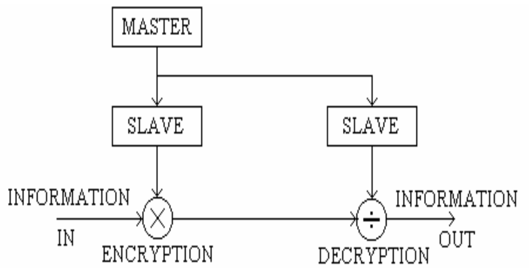

Fig. (1) Block scheme of a communication based on the synchronization of two chaotic systems

As optical fibers has already become a very important transmission medium and they have a great perspective, all-optical systems are advantageous compared to electrical ones. Taking this into account, the building blocks of the communication scheme in Fig. 1 are proposed ring optical cavities with a nonlinear optical medium inside (Fig. 2).

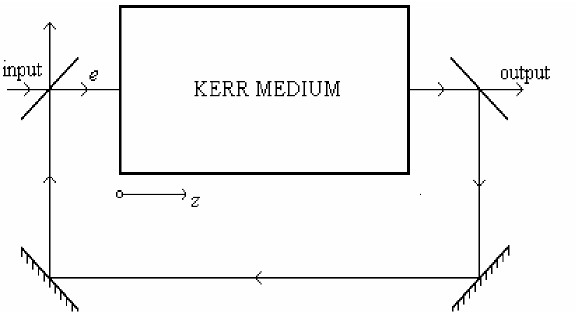

Fig. 2. Optical ring cavity configuration. The upper mirrors have reflectivities<1, whereas the lower ones are perfect reflectors

The nonlinear medium is a Kerr material whose response is described by the Debye relaxation equation. When the relaxation time constant of the medium is much longer than the delay time of the feedback of light and the medium is thin enough so that the phase shift of the electric field and the dissipation are small, the cavity is ruled by the set of ordinary differential equations [7]:

$$\dot{e} = a - be + i(\phi - \phi_0)e \qquad (4a)$$

$$\dot{\phi} = -\phi + |e|^2 \qquad (4b)$$

In the above, e is proportional to the slowly varying envelope of the electric field inside the cavity at z=0, ϕ is proportional to the phase shift of the electric field across the Kerr medium and time is expressed in Debye relaxation time units. a is a measure of the incident electric field amplitude, b characterizes the dissipation and ϕ_0 is the mistuning parameter of the cavity. See Ref. [7] for precise definitions. Equations (4) are valid when the ratio of the transit time of the cavity and the time relaxation constant of Kerr medium, denoted as $\rho\varepsilon$ (ρ=1/b), is $\rho\varepsilon \ll 1$, with $\varepsilon \ll 1$.

The output electric field of the cavity, which is proportional to e, exhibits not only bistability [8,9], but also a sequence of periodic and chaotic-like dynamics, as shown in Fig. (3) for the parameters b=0.2, ϕ=4 and a varying in both directions.

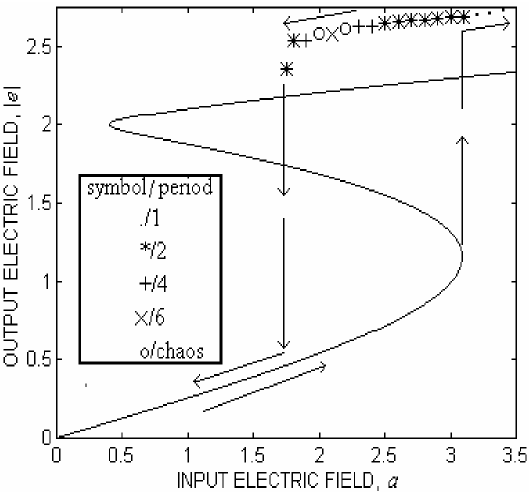

Fig. (3) Stationary states curve (solid curve) and actual dynamics (follow the arrows) of the optical cavity for b=0.2, ϕ_0=4, and *a* slowly sweeping in both directions. It can be seen that the system do not follow at all the upper branch of stationary states, but another one, composed of periodic orbits and chaotic ones. For the latter case, the temporal average of $|e|$ is plotted

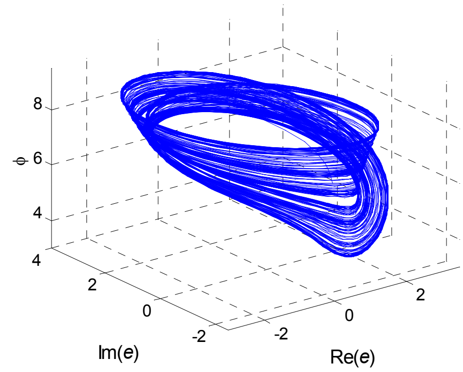

Fig. (4) Phase space representation of the chaotic dynamics of the optical cavity for *a*=2, *b*=0.2 and ϕ_0=4

We select the chaotic dynamics at a=2, completely establishing the master system at the transmitter. (Of course, an initial condition in the basin of attraction of the chaotic attractor is considered, not to get the other possible dynamics.) The chaotic attractor is presented in

Fig. (4). The dynamics is restricted to a quasi 2-dimensional manifold and it is interpreted as a result of the self-induced Rabi nutation of the electric field vector [7].

Below, the variables e and ϕ, as well as the parameters characterizing the master system will be written with the index 1. Indices 2 and 3 are reserved for the slave systems at the transmitter and receiver, respectively. Hence, the equations describing the communication scheme are:

$$\dot{e}_1 = a_1 - b_1 e_1 + i(\phi_1 - \phi_{01})e_1 \quad (5a)$$

$$\dot{\phi}_1 = -\phi_1 + |e_1|^2 \quad (5b)$$

$$\dot{e}_2 = \exp(i\rho\varepsilon\phi_1)c_{12}e_1 - b_2 e_2 + i(\phi_2 - \phi_{02})e_2 \quad (5c)$$

$$\dot{\phi}_2 = -\phi_2 + |e_2|^2 \quad (5d)$$

$$\dot{e}_3 = \exp(i\rho\varepsilon\phi_1)c_{13}e_1 - b_3 e_3 + i(\phi_3 - \phi_{03})e_3 \quad (5e)$$

$$\dot{\phi}_3 = -\phi_3 + |e_3|^2 \quad (5f)$$

The coupling of cavities 1 and 2 and 1 and 3, respectively, is introduced through the complex quantities c_{12} and c_{13} that include both the attenuation and the phase shift of the signals during propagation between cavities. To be in agreement with Pecora and Caroll synchronization method, the two slave systems are characterized by identical parameters.

The choice b_2=b_3=0.2, ϕ_{02}=ϕ_{03}=4, c_{12}=c_{13}=0.2exp(0.2i) and $\rho\varepsilon$=0.01 gives synchronization as shown in Fig. (5). On the average, the synchronization errors decay exponentially.

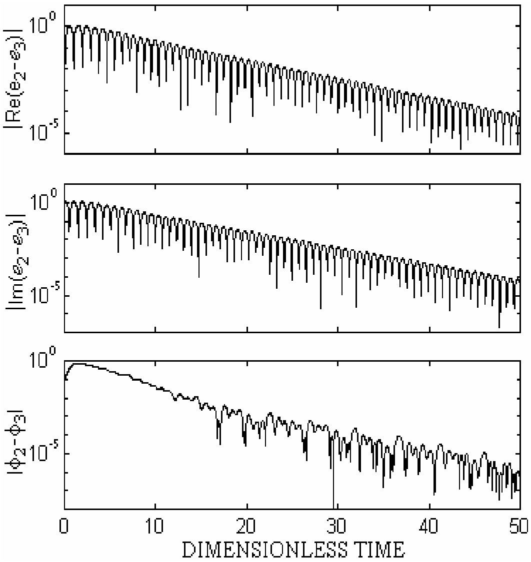

Fig. (5) Synchronization of optical cavities 2 and 3 both driven by the output signal from cavity 1. The values of the parameters are a_1=2, b_1=0.2, ϕ_{01}=4, $\rho\varepsilon$=0.01, b_2=b_3=0.2, ϕ_{02}=ϕ_{03}=4 and c_{12}=c_{13}=0.2exp(0.2i)

Numerical simulations prove that synchronization holds for any initial conditions and large ranges of parameter values. Besides, the synchronization is robust with respect to deviations from the identity of the slave systems up to about 10% in the parameter values. Parameters that may have significant different values are the coupling coefficients c_{12} and c_{13}. Figure (6) shows that synchronization errors stabilize at tiny values for c_{12} and c_{13} slightly different.

4. Discussion

A good encryption is enabled by a chaotic in a high degree of the carrier signal. This is given, for instance, by high values of the largest Lyapunov exponent and a high entropy [10]. Of special interest here is the mutual information of signal driving the slave system at transmitter and carrier signal. Taking the modulus of the electric field wave as signal, the plot $|e|_2$ versus $|e|_1$ is given in Fig. (7) and shows a small correlation of the two signals. The mutual information calculated based on the algorithm first proposed in Ref. [11] is about 2 bits, leading to a tough interception of the information.

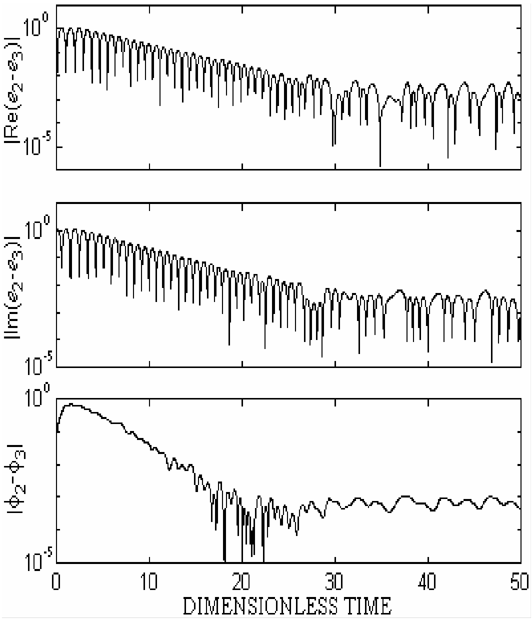

Fig. (6) Synchronization of optical cavities 2 and 3 when c_{13}=1.05c_{12}. All the other values of the parameters are as in Fig. (5)

The form of the carrier wave signal makes it suitable for an analog information signal. Frequency bandwidth of the carrier signal is about the reciprocal of time relaxation constant of Kerr medium. For instance, in case of carbon sulphide this quantity is of the order of 10^{12}Hz.

A specific model [Eqs. (4)] of the optical ring cavity has been investigated. For an improved modelling of the interaction processes in the system, see Refs. [12,13] for quantum formalisms of the interaction of an electromagnetical (optical) field with atomic media. Upper bound limit of transmission capacity is determined by quantum noise [14] establishing the theoretical limit of performances. Additional difficulties appear for the noise treatment in case of a carrier optical originating from a source with both optical and atomic coherence weights dependent on the operation conditions of the source.

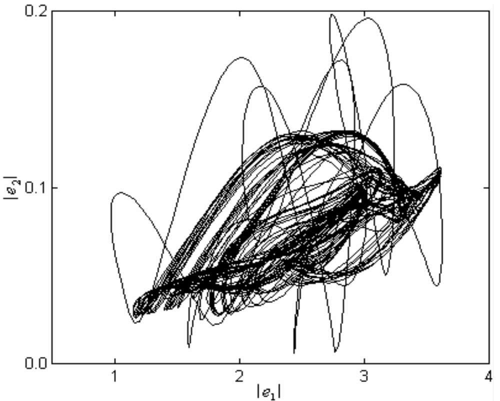

Fig. (7) $|e|_2$ **vs.** $|e|_1$**. Same parameter values as in Fig. (5)**

Masking digital information needs random sequences of pulses separated through large time intervals where the amplitude signal is very small. This kind of chaotic signals is available from other optical systems like semiconductor lasers with injection current modulation [15], where a modulation frequency in the GHz range ensures a good transmitting speed for the bits. A semiconductor laser with external cavity is expected to be used in information encoding at much higher bit rates.

5. Conclusion

In conclusion, we have demonstrated that masking the information in a chaotic optical wave from a nonlinear ring cavity is technically feasible in a secured communication system.

References

[1] L.M. Pecora and T.L. Caroll, *Phys. Rev. A* 44(4) (1991) 2374-2383.

[2] S. Hayes, C. Grebogy and E. Ott, *Phys. Rev. Lett.*, 70(20) (1993) 3031-3034.

[3] K.M. Cuomo and A.V. Oppenheim, *Phys. Rev. Lett.*, 71(1) (1993) 65-68.

[4] P. Colet and R. Roy, *Opt. Lett.*, 19(24) (1994) 2056-2058.

[5] U. Parlitz et al., *Phys. Rev. E*, 53(5) (1996) 4351-4361.

[6] P.M. Alsing et al., *Phys. Rev. E*, 56(6) (1997) 6302-6310.

[7] K. Ikeda and O. Akimoto, *Phys. Rev. Lett.*, 48(9) (1982) 617-620.

[8] I.M. Popescu, E. Stefanescu and P. Sterian, *Rev. Roum. Phys.*, 21(3) (1986) 221-235.

[9] P.E. Sterian, O. Rancu and I.M. Popescu, "Complex dynamics of radiation field in the transition area of optical bistability", in *Int. Conf. on Trends in Quantum Electronics, Proc. SPIE*, 1033 (1988) 154-157.

[10] G.L. Baker and J.P., Gollub, **"Chaotic Dynamics"**, Cambridge University Press, Cambridge (1990).

[11] A.M. Fraser and H.L. Swinney, *Phys. Rev. A*, 33(2) (1986) 1134-1140.

[12] P.E. Sterian, **"Fotonica"**, Bucuresti, Printech (2000).

[13] E. Stefanescu and P.E. Sterian, *Opt. Eng.*, 35(6) (1996) 153-155.

[14] P.E. Sterian, *Transmisia optica a informatiei*, Vol. I, II, Bucuresti, Editura Tehnica (1983).

[15] C.-H. Lee, T.-H. Yoon and S.Y. Shin, *Appl. Phys. Lett.*, 46(1) (1985) 95-97.

Quantum Limit Characterization of Signal-to-Noise Ratio using Phase-Shift Keying in Homodyne Detection

Nagham J. Shukur

[1] *Branch of Materials Science, School of Applied Sciences, University of Technology, Baghdad, Iraq*

In this work, a mathematical treatment for the quantum limit of signal-to-noise ratio (SNR) in homodyne coherent detection was presented. This treatment is based on the case of balanced detection when the incident signal power is much lesser than the local oscillator power when the efficient AC coupling is assumed. The final results were obtained from an analytical expression of SNR dependent of the average number of incident photons and the quantum efficiency.

Keywords: Phase-shift keying, DPSK, Homodyne detection, SNR, Balanced detection
Received: 15 December 2009, **Revised**: 24 March 2010, **Accepted**: 31 March 2010

1. Introduction

Although coherent detection is relatively new in optical communications, it has been around in radio communications for a long time. In both radio and optical communications, the essence of coherent detection is to generate a product term of the received signal and a local carrier. As a result, the received passband signal can be demodulated or shifted back to baseband. As an example, consider a passband signal $m(t)\cos(\omega_{inc}t)$ shown in Fig. (1a) [1].

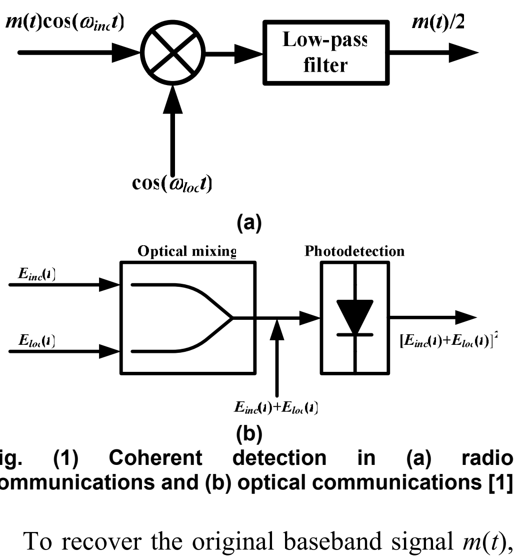

Fig. (1) Coherent detection in (a) radio communications and (b) optical communications [1]

To recover the original baseband signal $m(t)$, the received signal is multiplied by a local oscillator $\cos(\omega_{loc}t)$. If the local carrier is synchronized to the received signal $m(t)\cos(\omega_{inc})$ in frequency, i.e., $\omega_{inc}=\omega_{loc}$, the product term is [2]

$$m(t)\cos(\omega_{inc}t)\times\cos(\omega_{loc}t)=\frac{1}{2}m(t)+\frac{1}{2}m(t)\cos(2\omega_{inc}t) \qquad (1)$$

Therefore, the baseband signal can be recovered using the low-pass filter. The above mentioned scheme is called ***homodyning*** because $\omega_{inc}=\omega_{loc}$.

Both phase-shift keying (PSK) and differential phase-shift keying (DPSK) use signal constellations consisting of number of points equally spaced on a circle. While PSK encodes each block of logarithmic number of points (bits) in the phase of the transmitted symbol, DPSK encodes each block of the same logarithmic number of points (bits) in the phase change between successively transmitted symbols [3]. Tonguz and Wagner [4] showed that the performance of DPSK with optical amplification and interferometric detection is equivalent to standard differentially coherent detection [5].

Although the use of the multiplier to generate the product term is common in radio communications, it is not practical in optical communications [6]. An alternative way is to mix the incident signal with a local optical carrier. As illustrated in Fig. (1b), if the two signals have the same polarizations, the magnitudes of their fields can be scalar added. In this case, because the photocurrent output is proportional to the combined intensity,

$$I_{ph}=R\left\{P_{inc}+P_{loc}+2\sqrt{P_{inc}P_{loc}}\cos\left(\omega_{inc}t-\omega_{loc}t\right)\right\} \qquad (2)$$

where R is the responsivity of the photodiode and P_{loc} is the local oscillator power

Among three terms, P_{loc} is a constant term that can be simply filtered out by AC-coupling. The third term is the product term of interest. Because $P_{loc} >> P_{inc}$, $(P_{inc}P_{loc})^{1/2}$ is much larger than P_{inc}. Therefore, the latter term can be dropped.

A detailed block diagram of coherent homodyne detection is shown in Fig. (2). in homodyne detection, the carrier recovery loop uses a photodetector output to drive the carrier loop. The photodetector output carries the phase difference information of the signal and the local oscillator [1].

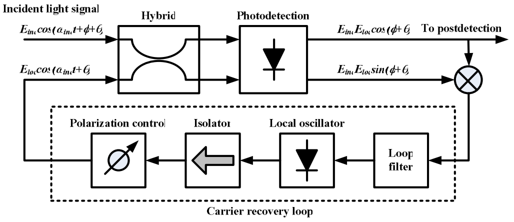

Fig. (2) Block diagram of homodyne coherent detection

2. Mathematical Treatment

Hybrid is a four-port device that mixes two light signals and, in general, its two inputs and two outputs are related by a 2x2 matrix as [7]:

$$\begin{bmatrix} E_{o1} \\ E_{o2} \end{bmatrix} = \begin{bmatrix} T_1 & X_1 \\ X_2 & T_2 \end{bmatrix} \begin{bmatrix} E_{inc} \\ E_{loc} \end{bmatrix} = \overline{H} \begin{bmatrix} E_{inc} \\ E_{loc} \end{bmatrix} \quad (3)$$

In coherent detection, there are two important types of hybrids that deserve further consideration. The first type is called the 180° hybrid, with the transfer matrix given by [1]:

$$\overline{H}_{180} = \frac{1}{\sqrt{2}} e^{i\theta} \begin{bmatrix} 1 & 1 \\ 1 & -1 \end{bmatrix} \quad (4)$$

There is a 180° phase shift between T_1 and T_2, and the hybrid is lossless because of

$$|T_1|^2 + |X_2|^2 = |T_2|^2 + |X_1|^2 = 1$$

The other important type of hybrid has a transfer matrix given by

$$\overline{H}_{90} = \frac{a}{\sqrt{2}} e^{j\theta} \begin{bmatrix} 1 & 1 \\ 1 & j \end{bmatrix} \quad (5)$$

where $0<a<1$ is a certain loss factor from practical implementation

This hybrid is called the 90° hybrid because there is a 90° phase shift between T_1 and T_2. In practical 90° four-port hybrid design, the loss factor (a) cannot be greater than 0.7071 because of the limitation of physics. This implies at least a 3dB power loss and is undesirable [1,8].

After the two light signals are mixed by the hybrid, there are two main configurations used in photodetection: single detection and balanced detection, which is illustrated in Fig. (3). Single detection uses only one photodiode and this is the same as in incoherent detection. In this case, one of the hybrid's outputs is not used and can be used for carrier recovery. Balanced detection feeds the two outputs to two photodiodes whose current outputs are subtracted. One major advantage of balanced detection is that it cancels the relative intensity noise (RIN) from the local oscillator [9].

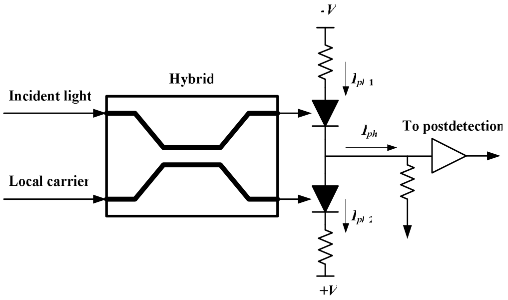

Fig. (3) Balanced detection

Consider the use of a 180° hybrid, the two outputs from the hybrid can thus be expressed as

$$E_{o1} = \frac{1}{\sqrt{2}}\left(E_{inc} + E_{loc}\right) \quad (6a)$$

$$E_{o2} = \frac{1}{\sqrt{2}}\left(E_{inc} - E_{loc}\right) \quad (6b)$$

After photodetection,

$$I_{ph,1} = \frac{R}{2}\left\{P_{inc} + P_{loc} + 2\sqrt{P_{inc}P_{loc}}\cos\left[\left(\omega_{inc} - \omega_{loc}\right)t + \phi(t)\right]\right\} \quad (7a)$$

$$I_{ph,2} = \frac{R}{2}\left\{P_{inc} + P_{loc} - 2\sqrt{P_{inc}P_{loc}}\cos\left[\left(\omega_{inc} - \omega_{loc}\right)t + \phi(t)\right]\right\} \quad (7b)$$

where P_{inc} is the incident light power and P_{loc} is the local carrier power

In amplitude modulation, P_{inc} is modulated according to the transmitted data. Also, $\phi(t)$ is the phase of the carrier and can be used for phase modulation [1,10]. With balanced detection, the difference between the photocurrents is

$$\begin{aligned} I_{ph} &= I_{ph,1} - I_{ph,2} \\ &= 2R\sqrt{P_{inc}P_{loc}}\cos\left[\left(\omega_{inc} - \omega_{loc}\right)t + \phi(t)\right] \end{aligned} \quad (8)$$

This subtracted current has no DC terms and is twice that of the individual photodiode output. Therefore, use of single detection has a 3dB (factor 1/2) power loss compared to balanced detection.

3. Results and Discussion

Based on the balanced detection, when homodyne detection is used or $\omega_s=\omega_{loc}$, then

$$I_{ph}=2R\sqrt{P_{inc}P_{loc}}\cos[\phi(t)] \tag{9}$$

In the case of homodyne detection, the photocurrent signal given by Eq. (9) is a baseband signal and immediately ready for detection. Specifically, as shown in Fig. (4), the photocurrent output from homodyne detection is first equalized by a matched filter and then followed by threshold detection. When the shot noise is approximated as Gaussian and there is no inter-symbol interference (ISI), this match filtering structure gives the optimum detection performance. When the input pulse is rectangular or a non-return-to-zero (NRZ) pulse, the matched filtering is equivalent to integrate-and-dump [11].

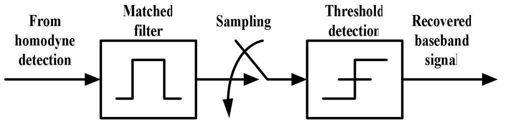

Fig. (4) Postdetection for homodyne detection

The current outputs given in Eqs. (7a) and (7b) contain only signal terms. In practice, there are additional noise terms that need to be added. In addition to receiver noise, two important noise terms are the shot noise from photodetection and the RIN from the local oscillator. Because the RIN power is proportional to the local optical power, which is much larger than the received signal power, the RIN can greatly affect detection performance. When balanced detection is used, the same RIN occurs at the two photodiode outputs. Therefore, by subtracting the two current outputs from balanced detection, the RIN can be cancelled [4,12].

After the RIN is cancelled, the only noise term to consider the shot noise because of the high local optical power. The two-sided power spectral density (PSD) of noise at each photodiode output is [1]

$$S_{n,i}(\omega)=\frac{1}{2}qRP_{loc} \tag{10}$$

where i is either 1 or 2

When the two current outputs are subtracted in balanced detection, the total noise power is

$$S_{n,i}(\omega)=S_{n,1}(\omega)+S_{n,2}(\omega)=qRP_{loc}B \tag{11}$$

Shot noise can be assumed to be Gaussian when the noise power is large [13-14]. If an integrate-and-dump filter is used in Fig. (15.6) as the matched filter for homodyne detection, the noise power at the threshold detector input is

$$\sigma_n^2=qRP_{loc}T \tag{12}$$

From Eqs. (9) and (12), the signal-to-noise ratio (SNR) in homodyne detection is given by

$$SNR=\frac{\left(2R\sqrt{P_{inc}P_{loc}}T\right)^2}{qRP_{loc}T}=\frac{4\eta P_{inc}T}{hf}=4\eta N \tag{13}$$

where N is the average number of incident photons over the period T, η is the quantum efficiency, and $R=q\eta/hf$

A SNR of 36 is needed to achieve a bit error rate (BER) of 10^{-9} for phase-shift keying (PSK) (ϕ=0 or π in Eq. (9)). If η=1, N must equal ($P_{inc}T/hf$)=9 photons per bit, which is the quantum limit using PSK homodyne detection [15].

As shown in Fig. (5), signal-to-noise ratio (SNR) is varying with the incident signal power (P_{inc}) at different responsivities. It is clear that the higher responsivity dump the noise to very small levels (negligible) as the incident signal power is increased with assumption of constant local oscillator power (P_{loc}).

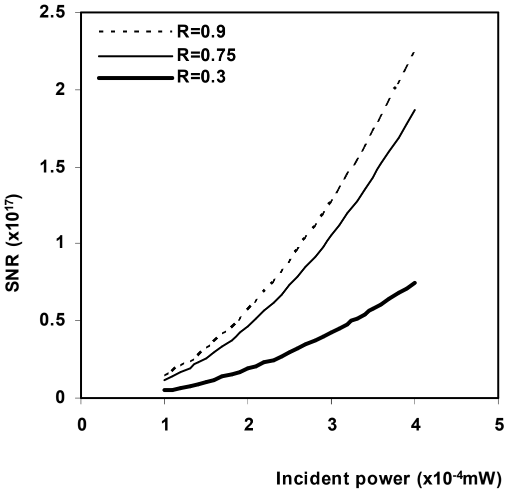

Fig. (5) Variation of SNR with incident power (P_{inc}) at different responsivities

Figure (6) shows that the shorter period taken by the incident photons to reach the detecting element is leading to undesirable levels of noise within the whole detection system. Therefore, it is important to control this period in order to prevent the noise from dominate the output signal or at least to limit the noise at rather acceptable levels not affecting the bit rate toward decrease. However, operating at very long periods may cause to stimulate some other types of noise those are not desirable at all in such detection systems [16].

It seems that there is no limit for increasing the number of incident photons per bit versus SNR, as shown in Fig. (7), at the low rates (<100photons/bit) as these photons are contributing to the output signal with low noise level. However, SNR does not reach very high levels despite the further increasing in the number of incident photons per bit because of the output signal saturation, which is an important limitation in such optoelectronic devices and systems.

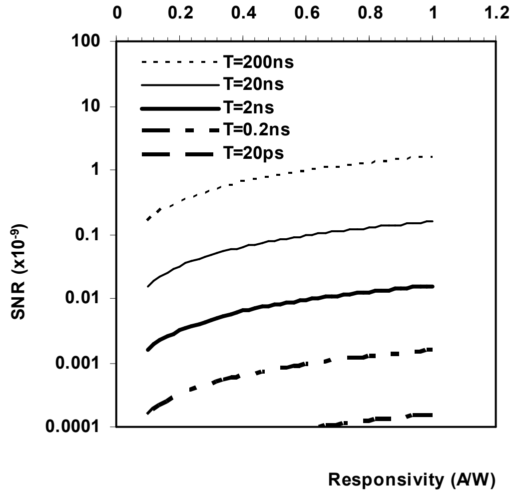

Fig. (6) Variation of SNR with responsivity (*R*) at different periods

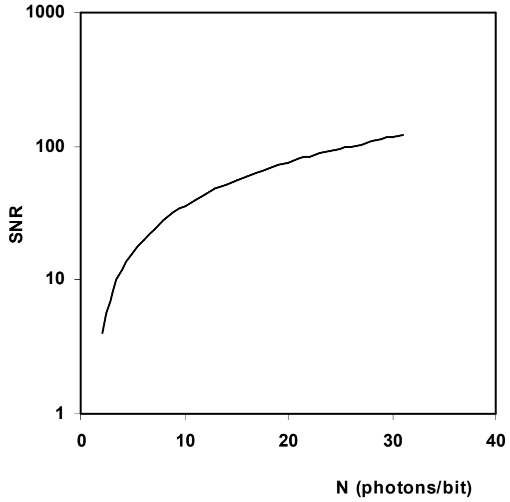

Fig. (7) Variation of SNR with number of incident photons (*N*)

4. Conclusion

From the results obtained in this work, the quantum limit of signal-to-noise ratio (SNR) in homodyne coherent detection was introduced. The behavior of SNR as a function of several parameters, such as incident signal power, responsivity and number of incident photons per bit, was explained for the case of balanced detection when the incident signal power is much lesser than the local oscillator power ($P_{loc}>>P_{inc}$) with the assumption of efficient AC coupling. In conclusion, the SNR can be expressed in terms of number of incident photons per bit and the quantum efficiency for an acceptable level as $4\eta N$.

References

[1] M.M.-K. Liu, **"Principles and Applications of Optical Communications"**, McGraw-Hill Co., Inc. (Chicago, U.S.A) (1996), Ch. 15, 754-770.

[2] A.R. Chraplyvy, *IEEE J. of Lightwave Technol.*, 8(10) (1990) 1548-1557.

[3] O.K. Tonguz and R.E. Wagner, *IEEE Photon. Technol. Lett.*, 3 (1991) 835-837.

[4] J.G. Proakis, **"Digital Communications"**, 4th ed., McGraw-Hill (2000).

[5] D.M. Kuchta and C.J. Mahon, *IEEE Photon. Technol. Lett.*, 6(2) (1994) 288-290.

[6] D. Marcuse, *IEEE J. of Lightwave Technol.*, 9(4) (1991) 505-513.

[7] S. Walklin and J. Conradi, *J. of Lightwave Technol.*, 17 (1999) 2235–2248.

[8] J. Wang and J.M. Kahn, *J. Lightwave Technol.*, 22(2) (2004) 362–371.

[9] P.S. Henry, “Error-rate performance of optical amplifiers”, *Proc. of Conf. on Optical Fiber Commun.*, Washington, DC, 1989, p. 170.

[10] P.A. Humblet and M. Azizoglu, *J. Lightwave Technol.*, 9 (1991) 1576–1582.

[11] J. Rebola and A. Cartaxo, *Proc. of SPIE*, 4087 (2000) 49–59.

[12] B. Jorgensen, B. Mikkelsen and C. Mahon, *J. Lightwave Technol.*, 10 (1992) 660–671.

[13] C.P. Kaiser, P.J. Smith and M. Shafi, *J. Lightwave Technol.*, 13 (1995) 525–533.

[14] S. Norimatsu and K. Iwashita, *J. Lightwave Technol.*, 10 (1992) 341–349.

[15] J.R. Barry and J.M. Kahn, *J. Lightwave Technol.*, 10 (1992) 1939–1951.

[16] J.D. Berger, Y. Zhang, J.D. Grade, H. Lee, S. Hrinya, H. Jerman, A. Fennema, A. Tselikov, and D. Anthon, “Widely tunable external cavity diode laser using a MEMS electrostatic rotary actuator”, Proc. of 27th Euro. Conf. on Optical Commun. Amsterdam, Netherlands, Sept. 30-Oct. 4, 2001.

Polynanocrystalline $CuIn_3Se_5$ Thin Film Photoabsorber Layer Produced by Pulsed-Laser Deposition

Anatoly Tverjanovich [1]
Sergey Bereznev [2]
Eugene Borisov [1]

[1] *Saint-Petersburg State University, 198504 Saint-Petersburg, Staryi Petergof, Ul'yanovskaya 5, Russia*
[2] *Tallinn University of Technology, Ehitajate tee 5, 19086 Tallinn, Estonia*

Polycrystalline bulk $CuIn_3Se_5$ samples for pulsed laser deposition (PLD) targets were synthesized in evacuated quartz ampoules by vacuum melting of 99.999% pure elements. All the polynanocrystalline $CuIn_3Se_5$ thin films were deposited onto the glass and glass/ITO substrates by using the PLD technique. The synthesized bulk samples and deposited films were tested by using the XRD analysis. The time–temperature regime of PLD process was developed for preparation of polynanocrystalline $CuIn_3Se_5$ thin films with the same composition as the source target. We have used advanced 3-stages temperature-time regime. The thickness of prepared $CuIn_3Se_5$ layers was in the range from 300nm till 450nm. The influence of the thermal annealing on the photovoltaic properties and morphology of the as-deposited $CuIn_3Se_5$ layers was investigated. The technique of preparation of high photosensitive polynanocrystalline thin $CuIn_3Se_5$ films of n-type conductivity was elaborated.

Keywords: Polycrystalline films, PLD, Photoabsorber layer, $CuIn_3Se_5$ films
Received: 28 January 2010, **Revised**: 09 March 2010, **Accepted**: 16 March 2010

1. Introduction

$CuIn_3Se_5$ is a promising photoabsorber of n-type of conductivity [1,2] for solar cells due to band gap value about 1.3eV [3] that is close to the optimal value of 1.4eV and high photoconductivity over a broad wavelength range [2]. On the other hand, this compound is less studied in comparison with $CuInSe_2$ in the pseudo-binary system Cu_2Se-In_2Se_3 [4]. Moreover, this compound was mainly investigated in a bulk state and only few papers described preparation and characterization the thin films fabricated by flash evaporation technique [1,3].

The main purpose of present work was preparation and investigation of polynanocrystalline $CuIn_3Se_5$ thin films and optimization of the deposition technique for solar cell application. We demonstrate formation of high-quality polynanocrystalline $CuIn_3Se_5$ photoabsorber layers grown on glass/ITO substrates by using the pulsed laser deposition (PLD) technique. Photovoltaic (PV) properties with both as-deposited and annealed $CuIn_3Se_5$ layers are studied.

2. Experiment

Polycrystalline bulk $CuIn_3Se_5$ samples for the PLD targets were synthesized from 99.999% pure elements in evacuated quartz ampoules. Ampoules were inserted in a pipe furnace, heated up to 1100°C, kept at this temperature for 5 hours and then very slowly cooled down. The synthesized samples were tested using the XRD analysis carried out on DRON-3.0 diffractometer equipped with monochromatic FeK_α source.

The films were deposited by using the PLD technique in accordance with the method developed by us for the $CuInSe_2$ based films [5]. Ablation of the targets was carried out by using XeCl excimer laser. For preventing of decrease of the Se content in the film during the deposition on the heated substrate we have used advanced 3-stages temperature-time regime of deposition: at the first stage initial $CuIn_3Se_5$ film was deposited at room temperature of substrate, then deposition was stopped and deposited glassy film was heated up to temperature T_1 for crystallization, and finally deposition was continued at relatively lower temperature of substrate T_2. The value of T_2 could be lower then T_1 because in this case vapor condensed on already formed polynanocrystalline $CuIn_3Se_5$ film and therefore nucleation was not limitative stage for crystallization. The appropriate values of T_1 and T_2 were chosen in accordance with our previous results [5] (T_1=320°C, T_2=160°C).

It should be noted, that the ablation rate for $CuIn_3Se_5$ target was much higher in comparison with the $CuInSe_2$ target at the same power of excimer laser.

For the XRD measurement the $CuIn_3Se_5$ films were deposited onto glass substrates; for investigation of PV properties, the $CuIn_3Se_5$ films were deposited on the glass/ITO substrates. The layers thicknesses on glass/ITO wafers were determined by using optical measurements and microscopy observations. The average thickness of the deposited $CuIn_3Se_5$ films was about 300nm. The cross-section and surface morphology of the $CuIn_3Se_5$ layers were investigated by scanning electron microscopy (SEM), using a commercial high-resolution LEO SUPRA 35 microscope equipped with energy dispersive spectroscopy (EDS) analyzer.

All the electrochemical PV measurements were performed in standard three-electrode cell in 0.1M H_2SO_4 background solution using AUTOLAB PGSTAT 30 potentiostat/galvanostat. The aqueous based graphite suspension (Alfa Aesar) was used for the contacts preparation on the surface of $CuIn_3Se_5$ for the I-V measurements.

3. Results and discussion

At the above mentioned regime we obtained well crystallized $CuIn_3Se_5$ films, as it was confirmed by XRD (Fig. 1). Position of the main peak at interplanar distance of 3.33Å coincides with $CuIn_3Se_5$ and $CuInSe_2$ reference data [6]. XRD patterns of $CuIn_3Se_5$ and $CuInSe_2$ are very similar except for a few additional reflections of a small intensity [6].

Reflection from (112) plane was very intensive (Fig.1). It means that film had columnar growth with preferred orientation along (112) direction. Columnar structure could be arisen because the stream of plasma from the target was directed non perpendicular to the substrate [8]. It was done in order to increase thickness uniformity of the films (the angle was about 45 degrees).

The grain size of film crystals (D) was calculated using Scherrer's equation [9]:

$$D = \frac{0.94\lambda}{\beta \cos\theta} \qquad (1)$$

where λ is X-ray wavelength, β is the full width at half maximum (FWHM) in radian, θ is the Bragg angle

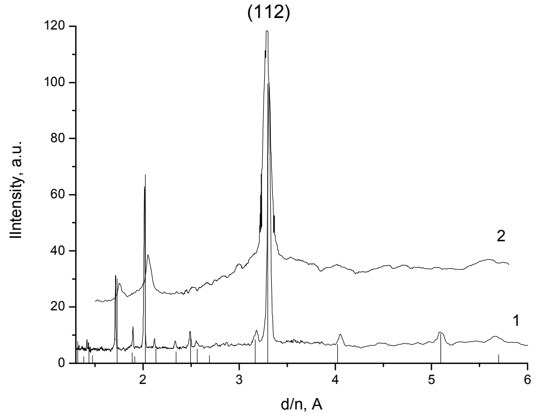

Fig. (1) X-ray diffractograms of $CuIn_3Se_5$ target (curve 1), deposited film (curve 2) and reference data for bulk $CuIn_3Se_5$ [7] (vertical lines)

The grain size value calculated from (112) reflex for the above mentioned sample was about 20nm. Analysis of composition of the as-deposited polycrystalline film with EDS showed small excess of In and small deficiency of Se against the stoichiometry (see Table 1, the second column). The similar composition was found for the films deposited at room temperature (in this case the films were glassy).

Table (1) Results of EDS analysis of as-deposited films and after various thermal treatments. The values in the brackets show the deviations in composition of samples vs. $CuIn_3Se_5$ stoichiometry

at.%	As-deposited	Annealing in air	Annealing in vacuum after contact with air	Annealing in vacuum chamber of the deposition setup
Cu	11,96 (+0,9)	13,82 (+2,7)	13,31 (+2,2)	15,47 (+4,4)
In	39,51 (+6,2)	35,89 (+2,6)	35,41 (+2,1)	34,64 (+1,3)
Se	48,52 (-7,0)	50,29 (-5,2)	51,28 (-4,2)	49,90 (-5,6)

Figure (2) shows that I-V curve of glass/ITO/$CuIn_3Se_5$ structure under chopped white light of 100mW/cm^2 intensity has non-linear character and demonstrates relatively high photosensitivity of the film

We had tried to enhance photovoltaic (PV) parameters of prepared photoabsorber films by additional thermal treatment under various conditions. Additional annealing in air at 450–500°C for 15–20min leaded to complete disappearing of the photoconductivity. Structure of the film became crumbly (Fig. 3b). For comparison, the structure of as-deposited film is represented in the Fig. (3a). Additional annealing in air leaded to oxidation of the film by the oxygen of air.

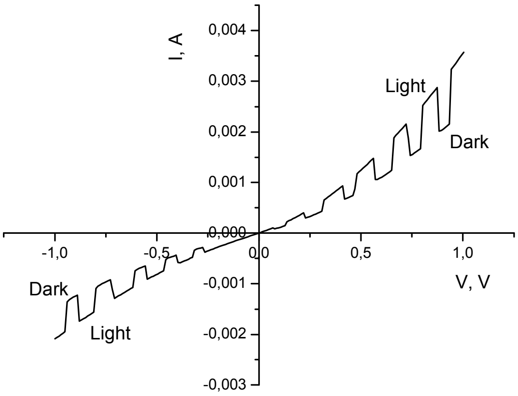

Fig. (2) I-V measurements of representative as-deposited $CuIn_3Se_5$ film under white light pulses of $100mW/cm^2$ intensity

It was found, that additional annealing in vacuum (after intermediate contact with air during the time of opening of the vacuum chamber) at 500°C for 30min leaded to decreasing of photoconductivity and linearity of I-V curve with a little higher current in direct region. Composition of the film became more similar to the stoichiometric composition, crystalline structure became more pronounced (Fig. 3c). According to our assumption, oxygen absorbed by the film surface partially oxidized the surface layer. At the same time the ordering of the crystal structure was improved. It has to be mentioned that the width of the $CuIn_3Se_5$ crystallites in Fig. (3c) is of about 50 to 200nm.

On the other hand, additional annealing in vacuum "in chamber" (immediately after the film deposition, without opening of the vacuum chamber) at 400°C for 20min leaded to increasing of photoconductivity, the shape of I-V curve became "like diode" (Fig. 4).

The shape of I-V curve confirmed the existence of Schottky junction between n-$CuIn_3Se_5$ and "like metallic" ITO layers. The SEM micrograph (Fig. 3d) shows the polynanocrystalline morphology of such prepared dense $CuIn_3Se_5$ films which include the interconnected grains with an average grain size of 50-100nm. It should be noted, that the formation of more equilibrium crystal structure of $CuIn_3Se_5$ photoabsorber layer resulted in increasing of photosensitivity.

The measurements of photoconductivity of the $CuIn_3Se_5$ film under chopped white light in background electrolyte confirmed high photosensitivity and n-type of conductivity of the deposited films. The photoelectrochemical characterizations for prepared CISe films were determined in 0.1M sulfuric acid background solution under chopped white light.

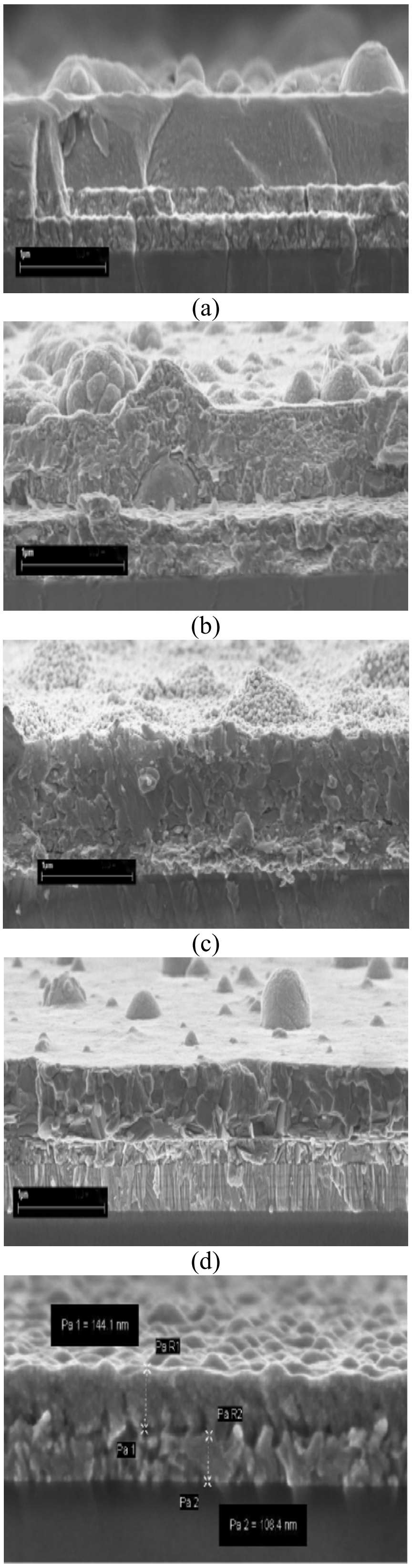

(a)

(b)

(c)

(d)

(e)

Fig. (3) SEM images of cross-sections of the $CuIn_3Se_5$ films: (a) as-deposited film; (b) film after annealing in air; (c) film after annealing in vacuum after contact with air; (d) film after annealing in vacuum chamber of the deposition setup; (e) image of $CuIn_3Se_5/CuInSe_2$ thin film sandwich structure

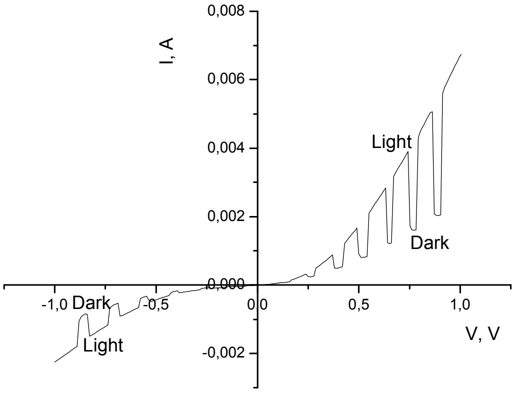

Fig. (4) I-V measurements of the deposited $CuIn_3Se_5$ film under white light pulses of 100mW/cm^2 intensity after additional annealing in vacuum chamber of the deposition setup

Figure (5) shows that obtained $CuIn_3Se_5$ films are photosensitive material and have the positive photocurrent in positive range of applied potential values. In the $CuIn_3Se_5$ electrode electron-hole pairs can be generated by light absorption. Therefore, photogenerated minority carriers are driven to the $CuIn_3Se_5$ surface by the electric field, at which they are consumed in photoelectrochemical processes. As it follows from the dependence, obtained films had the n-type of conductivity and could be applied as n-photoabsorber in complete cell structures. Thus, by adjusting the deposition temperature and post-deposition annealing "in chamber", nanostructured photosensitive $CuIn_3Se_5$ layers can be achieved.

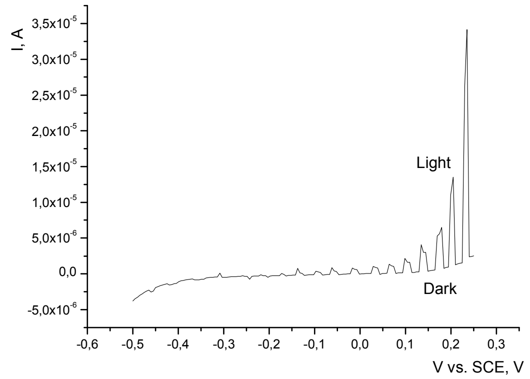

Fig. (5) I-V measurements in the electrochemical cell of the deposited $CuIn_3Se_5$ film after additional annealing in vacuum chamber of the deposition setup. Measurements were performed in 0.1M H_2SO_4 background solution vs. saturated calomel electrode (SCE) under white light pulses of 100mW/cm^2 intensity

One of the possibilities to increase the conversion efficiency of photovoltaic solar cells is creation of hybrid photovoltaic/thermal solar panels. A priory the optical properties of $CuIn_3Se_5/CuInSe_2$ thin film sandwich structure are optimal for such type devices. We prepared the $CuIn_3Se_5/CuInSe_2$ bi-layer structure by using developed PLD technique. The SEM cross section image of the structure is shown in Fig. (3e). Thickness of each layer was about 100nm. It is clearly seen polynanocrystalline structure of the deposited films. It should be noted, that mentioned structure is not yet optimized from the point of view of PV properties.

4. Conclusions

The technique of pulsed laser deposition of $CuIn_3Se_5$ films was developed and following thermal treatment allowed preparing of the high-photosensitive polynanocrystalline thin films of n-type conductivity. It was found, that additional annealing in vacuum (after the PLD process, without opening the vacuum chamber) leads to increasing of the photosensitivity and improving of polynanocrystalline structure of prepared $CuIn_3Se_5$ films. The best crystallinity of the $CuIn_3Se_5$ layers is attained at substrate temperatures ranging between 320°C and 400°C. With these characteristics $CuIn_3Se_5$ layers can be successfully applied for the preparation of heterojunction hybrid solar cells with controlled properties, as well as for the preparation of devices with controlled nanostructured donor-acceptor interfaces.

References

[1] G.E. Ariswan et al., *Solid State Commun.*, 124 (2002) 391.

[2] H.P. Wang, I. Shih and C.H. Champness, *Thin Solid Films*, 361-362 (2000) 494.

[3] P. Malar and S. Kasiviswanathan, *Solar Energy Mater. Solar Cells*, 85 (2005) 521.

[4] P. Malar and S. Kasiviswanathan, *Solar Energy Mater. Solar Cells*, 88 (2005) 281.

[5] A. Tverjanovich et al., *Solar Energy Mater. Solar Cells*, 90 (2006) 3624.

[6] U.C. Boehnke andG. Kuhn, *J. Mater. Sci.*, 22 (1987) 1635.

[7] H.P. Wang, I. Shih and C.H. Champness, *Thin Solid Films*, 361-362 (2000) 494.

[8] C. Buzea and K. Robbie, *J. of Optoelectron. Adv. Mater.*, 6 (2004) 1263.

[9] L.S. Birks and Friedman, *J. Appl. Phys.*, 16 (1946) 687.

Characterization of E-Mode InZnO Thin Film Transistors Produced by DC Sputtering Technique

Gamal M.A. Youssef
Ahmed M.H. El-Naggar
Amany S. Megazy

[1] *Department of Physics, Faculty of Sciences, Ain Shams University, Cairo, Egypt*

In this work, InZnO and InGaZnO were used as channel layers to fabricate enhancement mode thin film transistors on glass and flexible transparent substrate. The SiO_2-In_2O_3-ZnO system and N_2 plasma incorporated IZO film were grown to get a better controllability of the carrier concentration during the film growth. Hydrogen plasma and oxygen plasma effects on the TCO films and the TFTs were investigated.

Keywords: Thin Film Transistor, InZnO films, DC sputtering, ZnO devices
Received: 01 January 2010, **Revised**: 01 February 2010, **Accepted**: 01 March 2010

1. Introduction

Transparent conductive oxides (TCOs) were applied in many areas, such as the transparent electrodes used in liquid crystal displays, solar cells, and light emitting diodes because of their high electrical conductivity and high optical transparency [1-3]. Oxide-based thin film transistors attract much attention due to their advantages such as high mobility, high electrical conductivity, and high visible transmittance [4-7]. Amorphous or nano-crystalline n-type oxide semiconductors such as zinc oxide, zinc tin oxide, indium gallium oxide, and indium gallium zinc tin oxide displays demonstrate surprisingly high carrier mobilities (~10cm^2/Vs) even for amorphous films deposited at room temperature [8-11]. Many transparent thin film transistors (TTFTs) were reported using crystalline ZnO [12,13], or polycrystalline SnO_2 [14], and In_2O_3 [15]. However, to realize the transparent thin film transistor for flexible electronics, amorphous films are more suitable than crystalline type, because amorphous type oxide films have extra advantages such as low temperature deposition, good film smoothness, low compressive stress, and large area deposition by sputtering [16-18].

Among various conductive oxides, the IZO system exhibits many advantages for the flexible transparent TFTs such as high field effect mobility, high transparency, room temperature compatible process, large area deposition by sputtering, plastic substrates available, and is a cheaper process [6,20,22]. Other conductive oxides may not fit all the requirements for the flexible transparent TFTs. The first requirement is the film has to be transparent in visible region which means the bandgap E_g>3eV. CdO-PbO and $AgSbO_3$ systems have a bandgap smaller than this requirement [23,24]. The second requirement is the film must be amorphous and conductive as deposited in room temperature. CdO-CeO_2 is very resistive (resistivity ~1x10^{4}Ω.cm) [25] as deposited if no dopants are added in. In addition, Cd^{2+} ions is toxic against the environment [26]. Amorphous In_2O_3 looks like a good candidate, however, when the oxygen ratio increases a little bit, it becomes polycrystalline [27]. ZnO is always polycrystalline as deposited [22]. In_2O_3-ZnO systems have a wide range of amorphous materials in In/Zn ratio and various oxygen partial pressure [21,26]. Note that the change in oxygen ratio is very important because the carrier concentration can be adjusted by controlling the oxygen partial pressure or the O_2/Ar ratio. α-IZO has a considerable high mobility (10~50 cm^2/Vs) [22,28] as deposited at room temperature which is at least one order higher than amorphous Si [28]. Ga_2O_3-ZnO (GZO) system has a little bit lower mobility than IZO [22]. GaInZnO (GIZO) also has a little bit lower mobility compared to IZO [26]. The last candidate is ITO, which is widely used as electrodes in LEDs, solar cells and LCDs [29-31]. Compared to ITO, IZO has a higher work function [32,33], higher transmittance in the infrared region [34], and lower In concentration than ITO. A higher In concentration means higher price [33]. Accordingly, the IZO will be used as channels and electrodes to fabricate the flexible transparent TFTs in this research. GIZO-TFTs were reported having a better stability than IZO-TFTs [35]. Thus, GIZO-TFTs will also be included in this study.

2. Experiment

The enhance mode TFT structure is shown in Fig. (1a). We also plan to use IZO and IGZO as the channel layers and design structures for the channel. Recently, we successfully fabricated enhance mode thin film transistors using IZO as the channel layer as depicted in Fig. (1b). The device has very good performance which will be described later.

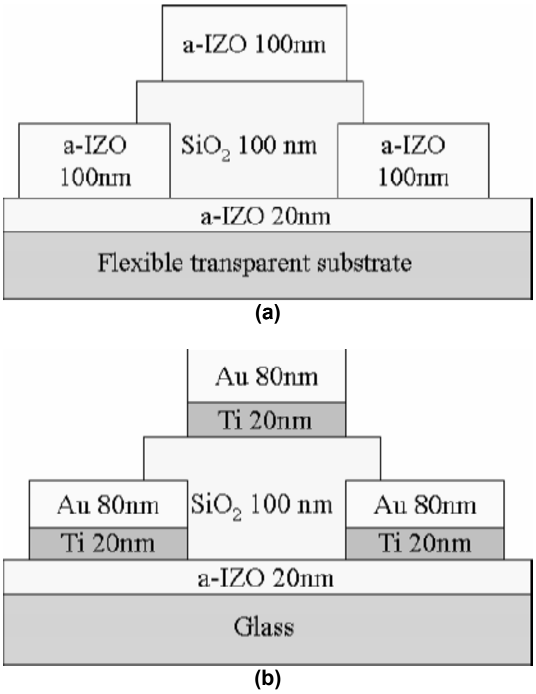

(a)

(b)

Fig. (1) (a) Schematics of the E-Mode TFTs on flexible transparent substrate and (b) E-Mode TFTs on glass

The IZO film was deposited in the sputtering machine with two targets, ZnO and In_2O_3, together with O_2 and Ar gas in the chamber. The O_2/Ar ratio decides the carrier concentration in the IZO film. Here we plan to use N_2/O_2/Ar gas mixture to deposit IZO film. The reasons to use N_2 is because in the plasma, N_2 will convert to N_2^+, which may replace O and bond with In. This was investigated in forming p-type ZnO [36]. We know the carriers in the IZO result from the non-stoichiometry, which means the lack of oxygen allows some In atoms that are not bonded with oxygen atoms to release electrons to the conduction band. That is why when the O_2/Ar ratio change during IZO film deposition, the carrier concentration will also change. Higher O_2/Ar ratio leads to a decrease in the number of oxygen vacancies, which also means the carrier concentration decreases [21]. When removing one oxygen atom from the indium, one oxygen vacancy is created. Indium is a big atom and tends to lose electrons. Oxygen is a small atom and tends to get electrons from the indium. ZnO acts as a stabilizer in the In_2O_3 matrix. That's why IZO and (GaZnO) GZO both have lower sensitivity of O_2/Ar ratio to carrier concentration than ZnO [22]. Since the oxygen has a higher electronegativity than nitrogen, oxygen can form a strong ionic bond with indium. This means when removing or adding a certain amount of oxygen or nitrogen bonded with indium, oxygen will produce a larger change in carrier concentration than nitrogen. This means nitrogen can reduce the sensitivity of O_2/Ar ratio to carrier concentration. The second reason is, due to the previous reason, nitrogen may improve the device reliability. A reliability issue is one of the reasons why GaInZnO was developed [35]. We may provide another view to do the same thing by an easier method.

Ga_2O_3 introduced into the In_2O_3-ZnO system to form the InGaZnO was reported as providing a better stabilization in TFTs than IZO [35]. Gallium was chosen because it has an atomic radius close to indium. The introduction of gallium into the IZO reduces the electron concentration and mobility. The highest carrier concentration of IGZO is around $\sim 10^{19}cm^{-3}$ [26] which is smaller than that of IZO ($\sim 10^{21}cm^{-3}$) [19,22]. The reduction in carrier concentration is not bad because for the channel layer, $10^{18}\sim 10^{16}cm^{-3}$ is enough for both depletion and enhancement mode TFTs. Although carrier concentration in IZO can also be adjusted by O_2/Ar ratio, the carrier concentration change in the IZO film is dramatic ranging from 10^{18} to $10^{16}cm^{-3}$ in a small O_2/Ar ratio region [21]. Gallium not only reduces carrier concentration, but also reduces the sensitivity of the carrier concentration to the O_2/Ar ratio [22,26]. It is good for controlling the carrier concentration. However, in the mean time, the reduction in mobility is not desired. It is interesting to introduce another oxide into the IZO system to stabilize the oxide system and the mobility. The idea is to incorporate a smaller atom and in the mean time, oxide formed by this atom has E_g>3eV. SiO_2 fits these requirements. Si can easily bond with oxygen to reduce sensitivity of the carrier concentration to the O_2/Ar ratio during film deposition. Also, due to the smaller radius of Si than Ga, In atoms still can keep their s orbitals overlapped. This means the mobility may not be degraded too much.

Due to the different interfaces that may form between IZO and various dielectrics, it is necessary to use different dielectrics such as SiO_2, SiN, and Sc_2O_3 as the gate dielectrics in the TFTs and compare the device performance.

O_2 plasma can obviously decrease the surface carrier concentration of the IZO film due to the annihilation of the oxygen vacancies. This might help to reduce the surface leakage and then improve on/off ratio if the surface leakage dominates the leakage current, especially for the depletion mode FET.

After we successfully fabricate the E-mode FETs, we can start to make a ring oscillator using these TFTs. The reliability test will include (i) current stress in room temperature and high temperature (ii) thermal shock and bending test. These tests will be applied to the TCO films and devices on both glass and PET. The device will also be measured for the s parameters and be simulated to extract the parasitic parameters of the D-mode and E-mode FETs. We have already performed the simulation for the D-mode IZO TFTs.

3. Results and Discussion

Enhancement mode top-gate TFTs using 20nm of *a*-IZO channels and 100nm thick SiO_2 gate insulators deposited by plasma-enhanced chemical vapor deposit ion (PECVD) were fabricated. Figure (1b) shows the cross-section structure of the TFT with a gate dimension of 1µm×100µm. The IZO film was deposited in 3.1% of O_2/Ar ratio has a carrier concentration about $1.5x10^{16}cm^{-3}$. The SiO_2 layer was deposited without heating the substrates, making the entire process consistent with typical continuous-use temperatures of commercial plastic films for electronic devices.

Figure (2) shows typical drain current versus drain voltage, I_{DS}-V_{DS}, characteristics from the IZO transistors. The transistor operates in enhancement-mode showing excellent pinch-off.

Figure (3) shows drain current, I_{DS}, and transconductance, g_m, as a function of V_{GS} for an IZO TFT. A transconductance of 10mS/mm was obtained at drain current of 0.3mA at 0.85V gate voltage and 3V drain voltage. The transistor has a low threshold voltage of 0.5V and an excellent sub-threshold voltage swing of 0.135V/decade. The drain current on-to-off ratio was ~10^5. The gate leakage is about 10^{-10}~10^{-9}A.

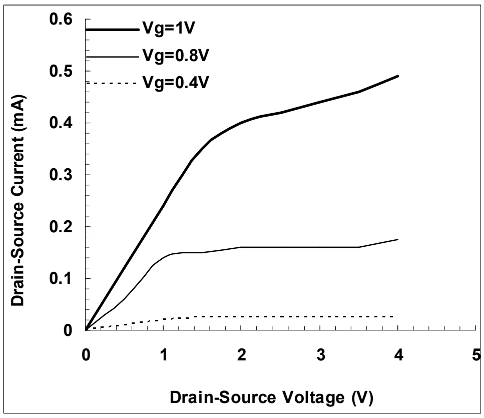

Fig. (2) Typical drain current versus drain voltage, I_{DS}-V_{DS}, characteristics from the IZO transistors

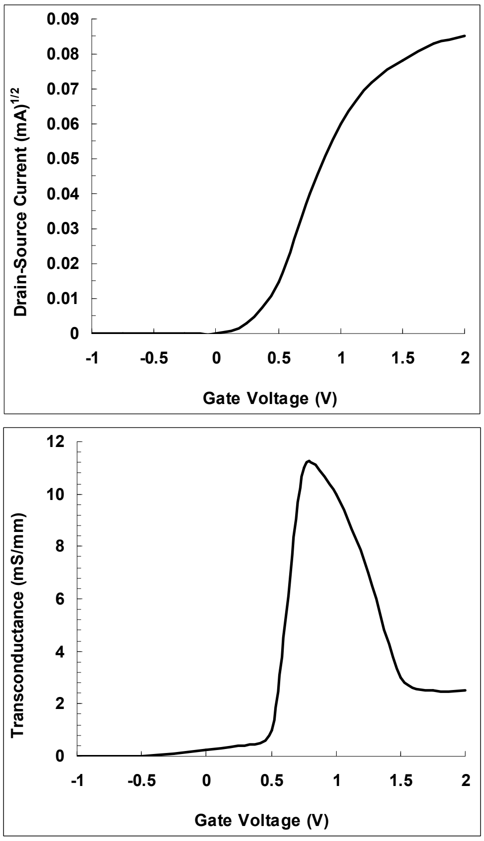

Fig. (3) Drain current, I_{DS}, and transconductance, g_m, as a function of V_{GS} for an IZO TFT

4. Conclusion

In this work, IZO and IGZO were used as channel layers to fabricate enhancement mode TFTs and ring oscillators on glass and flexible transparent substrate (PET). The SiO_2-In_2O_3-ZnO system and N_2 plasma incorporated IZO film were grown to get a better controllability of the carrier concentration during the film growth. Hydrogen plasma and oxygen plasma effects on the TCO films and the TFTs were investigated. The device reliability was tested to compare the effects from different TCO films and process treatments. Devices were simulated in a device model to extract the parasitic parameters.

Devices were characterized in dc and rf performance. The enhancement mode TFTs have been fabricated successfully on glass by using IZO films as the channel layers.

References

[1] A.K. Kullarni et al., *Thin Solid Films*, 308 (1997) 1.

[2] K. Zhang et al., *Thin Solid Films*, 376, 255, (2000).

[3] H. Kim et al., *J. Appl. Phys.*, 86, 6451 (1999).

[4] K. Nomura et al., *Nature*, 432, 288 (2004).

[5] E. Fortunato et al., *Appl. Phys. Lett.*, 85, 2541 (2004).

[6] N.L. Dehuff et al., *J. Appl. Phys.*, 97, 064505 (2005).

[7] E. Fortunato et al., *Adv. Mater.*, 17 590 (2005).

[8] J. Park et al., *J. Vac. Sci. Technol.*, B24, 2737 (2006).

[9] H.-H. Hsieh and C.-C. Wu, *Appl. Phys. Lett.*, 89, 041109 (2006).

[10] J. Siddiqui et al., *Appl. Phys. Lett.*, 88, 212903 (2006).

[11] P.F. Garcia, R.S. McLean and M.H. Reilly, *Appl. Phys. Lett.*, 88, 123509 (2006).

[12] P.F. Carcia et al., *Appl. Phys. Lett.*, 82, 1117 (2003).

[13] E. Fortunato et al., *J. Non-Cryst. Solids*, 338-340, 806 (2004).

[14] R.E. Presley et al., *J. Phys. D: Appl. Phys.,* 37, 2810 (2004).

[15] Dhananjay, C.W. Chu, *Appl. Phys. Lett.*, 91, 132111 (2007).

[16] H. Yabuta et al., *Appl. Phys. Lett.*, 89, 112123 (2006)

[17] T. Minami, *J. Vac. Sci. Technol.*, A17 (1999) 1765.

[18] T. Sasabayashi et al., *Thin Solid Films*, 445, 219 (2003).

[19] H.C. Pan et al., *J. Vac. Sci. Technol.,* A 23, 1187 (2005).

[20] Yu-Lin Wang et al., *Appl. Phys. Lett.*, 90, 1 (2007)

[21] W. Lim et al., *Electrochem. Solid-State Lett.*, 10, H267 (2007).

[22] R. Martins et al., *J. Appl. Phys.*, 101,044505 (2007).

[23] H. Hosono et al., *Appl. Phys. Lett.*, 68,29 (1996).

[24] M. Yasukawa et al., *Jpn. J. Appl. Phys.*, Part 2, 34, L281 (1995).

[25] S. Narushima et al., *J. Non-Cryst. Solids*, 374, 313 (2000).

[26] H. Hosono, *J. Non-Cryst. Solids*, 352, 851 (2006)

[27] H. Nakazawa et al., *J. Appl. Phys.*, 100, 093706 (2006)

[28] Y. Sun and J.A. Rogers, *Adv. Mater.*, 19, 1897 (2007).

[29] H. Fujikawa et al., *Appl. Phys. Lett.*, 70, 270 (1997).

[30] L. Davis, *Thin Solid Films*, 236,1 (1993).

[31] F. Benkhelifa et al., *Thin Solid Films*, 232, 83 (1993).

[32] J. Cui et al., *Adv. Mater.*, 31, 1476 (2001).

[33] B. Kumar and H. Gong, *J. Appl. Phys.*, 98, 073703 (2005).

[34] J.M. Philips et al., *Appl. Phys. Lett.*, 67, 2246 (1995).

[35] T. Kamiya et al., *J. Electroceram.*, 17,267 (2006).

[36] C.L. Perkins et al., *J. Appl. Phys.*, 97, 034907 (2005).

Profiling of Antimony Diffusivity in Silicon Substrates using Laser-Induced Diffusion Technique

Oday A. Hamadi

Department of Biological Sciences, College of Education, TheIraqi Islamic University in Baghdad, IRAQ

In this work, profiles of laser-induced diffusion of antimony in silicon were presented. These profiles were considered to attempt enhancing of the silicon-based devices. This enhancement is attributed to the increasing achieved in the diffusion length within a certain layer of the active region in the device. Laser-induced diffusion is a perfect technique for improving the characteristics of electronic devices since it is flexible, contactless, clean and well controlled.

Keywords: Laser-induced diffusion, Sb-doped silicon, Transistor current gain
Received: 06 January 2010, **Revised**: 22 February 2010, **Accepted**: 01 March 2010

1. Introduction

Employment of lasers in microelectronics fabrication and production is one of the most important fields of laser applications those received attention of academic and industrial works during the three last decades. First, lasers were used for annealing of materials in a manner not cause damage to the lattice after performance of ion implantation technique. Due to precise control of laser parameters, formation of extremely shallow junctions and redistribution of impurities in semiconductors became very flexible and reliable techniques with compared to the conventional ones [1-12].

Tendencies toward reducing the geometrical dimensions of electronic and integrated devices to improve their speed and power performance pushed photolithographic resolution to the limits regarding to horizontal dimensions. As well, vertical dimensions should be reduced to maintain device depths and more closely controlled dopant profiles. Normal thermal diffusion of shallow junctions requires one minute or little less for a typical dopant source. Raising the temperature of a semiconductor wafer to diffusion temperatures definitely causes some mechanical problems such as deformations in the solid structure. Such problems should be expected to cause variations in junction dimensions, which is forbidden in manufacturing and fabrication procedures especially when these variations degrade the requirements from such processes [1, 13-14].

Laser-induced diffusion (LID) offers excellent technique for fabrication of the shallow junctions. The heating and cooling rates of semiconductors by LID are 10^{10}-10^{12} °C/s and such rates are sufficient for impurity atoms to occupy substitutional sites in the substrate lattice. Such rates do not admit for diffuse to longer distances, thus LID technique provides very sharp diffusion profiles. Laser-induced diffusion technique has an advantage over all conventional techniques as it is performed without masks. Instead, use of optics for focusing laser beam with respect to the surface processed is perfect alternative [2].

As confirmed by recent works, application of dopant sources to the wafer in order to form junctions is followed by laser irradiation. There are several techniques used for deposition of dopant materials on the wafers such as vacuum evaporation, Si-based doping, spray pyrolysis and coatings. As well, dopants can be provided from the gas phase by using laser pulses for photo-decomposition above the surface of wafer and then another laser pulses to induce the diffusion of dopants into the surface of substrate [10-15].

In conventional IC processing, solid-state diffusion is an isothermal process as the substrate is heated uniformly to high temperatures (900-1300°C), so that the dopant atoms have sufficient energy to move through the lattice of substrate. Such process is emerging from the gradient in impurity concentrations that induces atoms to flow from the high-concentration regions towards those low [16]. Because laser irradiation is a localized heating process in three dimensions, it results a localized dopant flow. The diffusion coefficient (D) is determined as:

$$D = A\exp(-\frac{E_a}{KT}) \qquad (1)$$

where E_a is the activation energy of dopant atoms, K is Boltzman's constant and T is the temperature

Already, the diffusion depth is a function of depth (x) into surface as:

$$D(x) = D(0)\exp(-\alpha x) \qquad (2)$$

where the exponential term corresponds the normalized diffusion profile $D(x)/D(0)$

Both decay constant (α) and diffusion coefficient $D(0)$ are determined empirically.

2. Experiment

Substrates of (100) p-type silicon wafers were used as substrates. The dopant materials were antimony, arsenic or titanium of 99.99% purity but only the results of antimony were discussed due to their clearance. Silicon wafers were cleaned in HF solution, rinsed in deionized water, dried in nitrogen then immediately transferred to vacuum deposition system. The thickness of dopant was ~300nm and the wafers were classified into 3 groups due to dopant material. The samples were kept in a sealed vessel until transferred to be irradiated by laser. They were irradiated in air by 10ms pulses from a JK2000 1.06µm Nd:YAG laser system. The maximum power per laser pulse is 1kW with the TEM_{00} mode. Several optical lenses of different focal lengths were used for controlling laser beam size. The position of sample with respect to the laser beam could be varied by a *xy*-table, so the laser beam could scan the sample precisely.

3. Results and Discussion

As shown in Fig. (1), the normalized diffusivity profile decays exponentially with the distance into the substrate. Such decay corresponds a similar response of the optical absorption characteristics. Both decay constant (α) and the diffusivity at the surface ($D(0)$) should be determined empirically by fitting the obtained data of laser-generated profile. Hence, the flux (Φ) of dopants is given by:

$$\Phi = -\frac{\partial}{\partial x}[D(x).N(x,t)] \qquad (3)$$

Consequently, the doping concentration varying with time can be determined by:

$$\frac{\partial N(x,t)}{\partial t} = \frac{\partial \Phi}{\partial x} = -\frac{\partial}{\partial x}\left\{\frac{\partial}{\partial x}[D(x,t).N(x,t)]\right\} \qquad (4)$$

We intended to introduce the characteristics of impurity diffusion in silicon substrate. As shown in Fig. (2), the concentration of antimony atoms (C_{As}) diffused inside silicon substrate increases fast with increasing irradiation laser intensity then tends to be constant with increasing laser intensity. This might be attributed to the limits of solid solubility of Sb dopant in silicon (~2.25x10^{14}atoms/cm^3). Increasing the irradiation laser intensity would cause to exceed damage threshold of the bulk substrate. So, optimum diffusion of dopants can be achieved below a certain value of irradiation intensity.

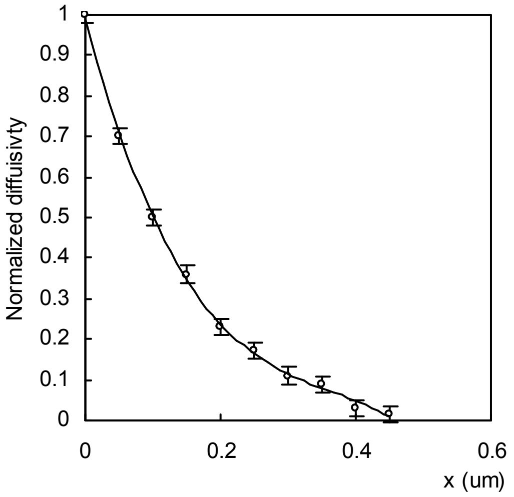

Fig. (1) The normalized diffusivity profile along the distance into the substrate

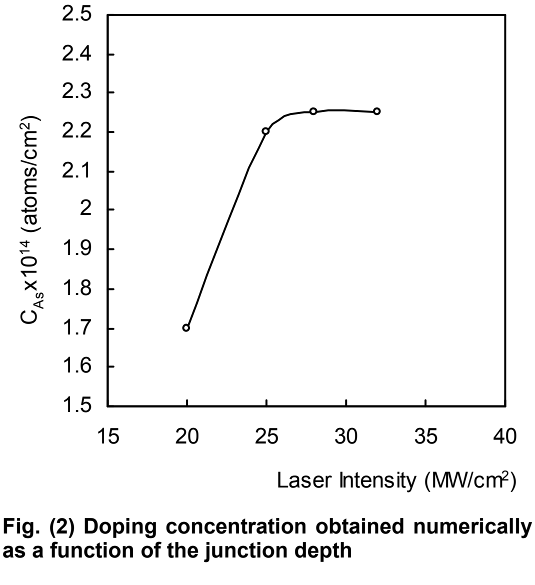

Fig. (2) Doping concentration obtained numerically as a function of the junction depth

To explain how to control the depth of the formed junction by the irradiation laser intensity, the junction depth was determined as a function of laser intensity. Although the increasing of depth is slow with increasing laser intensity, as shown in Fig. (3), it seems to be uniform relation, which is necessary to be considered as a control parameter.

The equation (4) was solved numerically using MATLAB software to obtain the profile of doping concentration as a function of junction depth into surface, as shown in Fig. (4). In order to introduce the variation of doping concentration (C_{doping}) along the depth into surface of silicon substrate, we have measured doping concentration with depth for three different irradiation intensities ($I_1<I_2<I_3$). It is obvious from Fig. (4) that doping concentration decreases with advance inside surface as well as the higher irradiation intensity induces dopants to penetrate deeper. This behavior in Fig. (4) agrees well with the normalized diffusivity in Fig. (1).

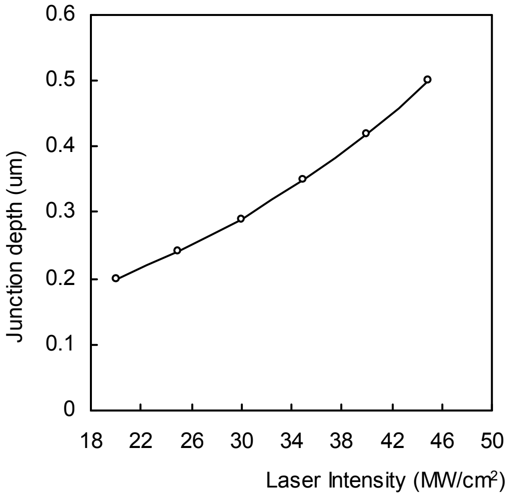

Fig. (3) Depth of the formed junction as a function of laser irradiation intensity

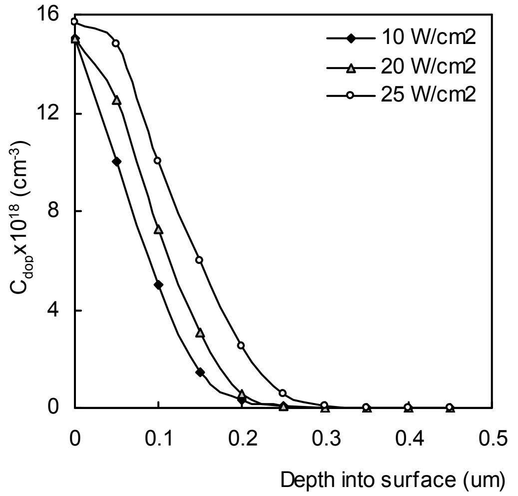

Fig. (4) The concentration of antimony atoms as a function of depth into surface at three different irradiation laser intensities (10, 20, and 25W/cm^2)

According to Eq. (2) and boundary conditions, we can determine the diffusivity of dopants as a function of irradiation laser intensity. As expected, the diffusivity increases linearly with increasing intensity to the maximum intensity used. The linearity enables to suppose that the profile of antimony doping is uniform which simplifies the numerical treatment of such variation. Results are shown in Fig. (5). Such increasing cannot be continuous as confirmed by the same equation due to the limitation of decay coefficient (α).

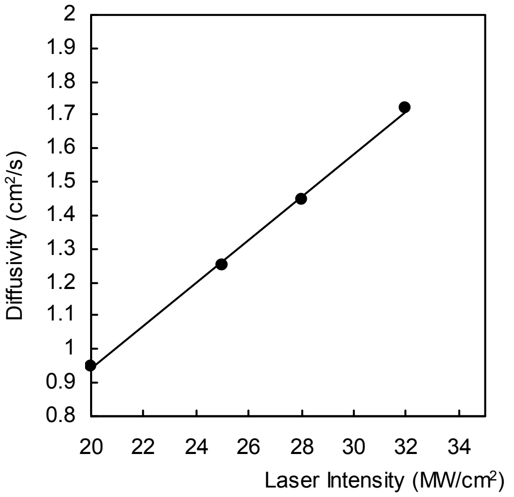

Fig. (5) The laser-induced diffusivity of Sb as a function of irradiation laser intensity. Though it is linearly increasing function but it is limited by the solid solubility of dopants

4. Conclusions

Due to results obtained in this work, diffusivity profiles of antimony dopants in silicon substrate were determined. The diffusion of dopants was induced by irradiation with pulsed laser. Laser-induced diffusion is a perfect technique for improving the characteristics of electronic devices since it is flexible, contactless, clean and well controlled.

References

[1] C.W. White and P.S. Peercy, **"Laser and Electron Beam Processing of Materials"**, Academic Press (NY) (1980) 468.

[2] J.M. Poate and W. Moyer, **"Laser Annealing of Semiconductors"**, Academic Press (NY) (1982) Ch.3, 4, 5, 6, 183.

[3] S. Cohen, P. Wyatt and G. Chapman, G., *IEEE Trans. Electron. Devices*, 38(9) (1991) 2042-2050.

[4] R.A. Ismail, "Study of induced diffusion and defects in germanium by pulsed laser", Ph.D. Thesis, University of Technology (1995).

[5] S. Mitha *et al.*, *Appl. Phys. Lett.*, 69 (1996) 922-924.

[6] P.G. Sanders and M.J. Aziz, *J. Appl. Phys.*, 86(8) (1999) 4251-4261.

[7] W.K. Hamoudi and R.O. Dala Ali, *J. Eng. & Technol.*, 19 (2000) 125-135.

[8] W.K. Hamoudi and R.O. Dala Ali, *J. Eng. & Technol.*, 19 (2000) 1-6.

[9] R.A. Ismail and A.A. Hadi, *Turk. J. Phys.*, 27 (2003) 1-8.

[10] W.K. Hamoudi and R.O. Mahdi, *Iraqi J. Appl. Phys.*, 1(1) (2005) 1-5.

[11] D. Auston *et al.*, *Appl. Phys. Lett.*, 34 (1979) 777-779.

[12] J. Narayan *et al.*, *Appl. Phys. Lett.*, 33 (1978) 338-340.

[13] R. Young, J. Narayan and R.F. Wood, *Appl. Phys. Lett.*, 35 (1979) 447-449.

[14] K. Affolter, W. Luthy and M. von Allmen, *Appl. Phys. Lett.*, 35 (1978) 185-187.

[15] T. Deutch *et al.*, "Pulsed UV laser photochemical doping of semiconductors", *Proceeding CLEO'8* (Washington) (1981) 110.

[16] R.M. Warner, Jr. and J.N. Fordenwalt, **"Integrated Circuits: Design, Principles and Fabrication"**, McGraw-Hill Book Co. (NY) (1965).

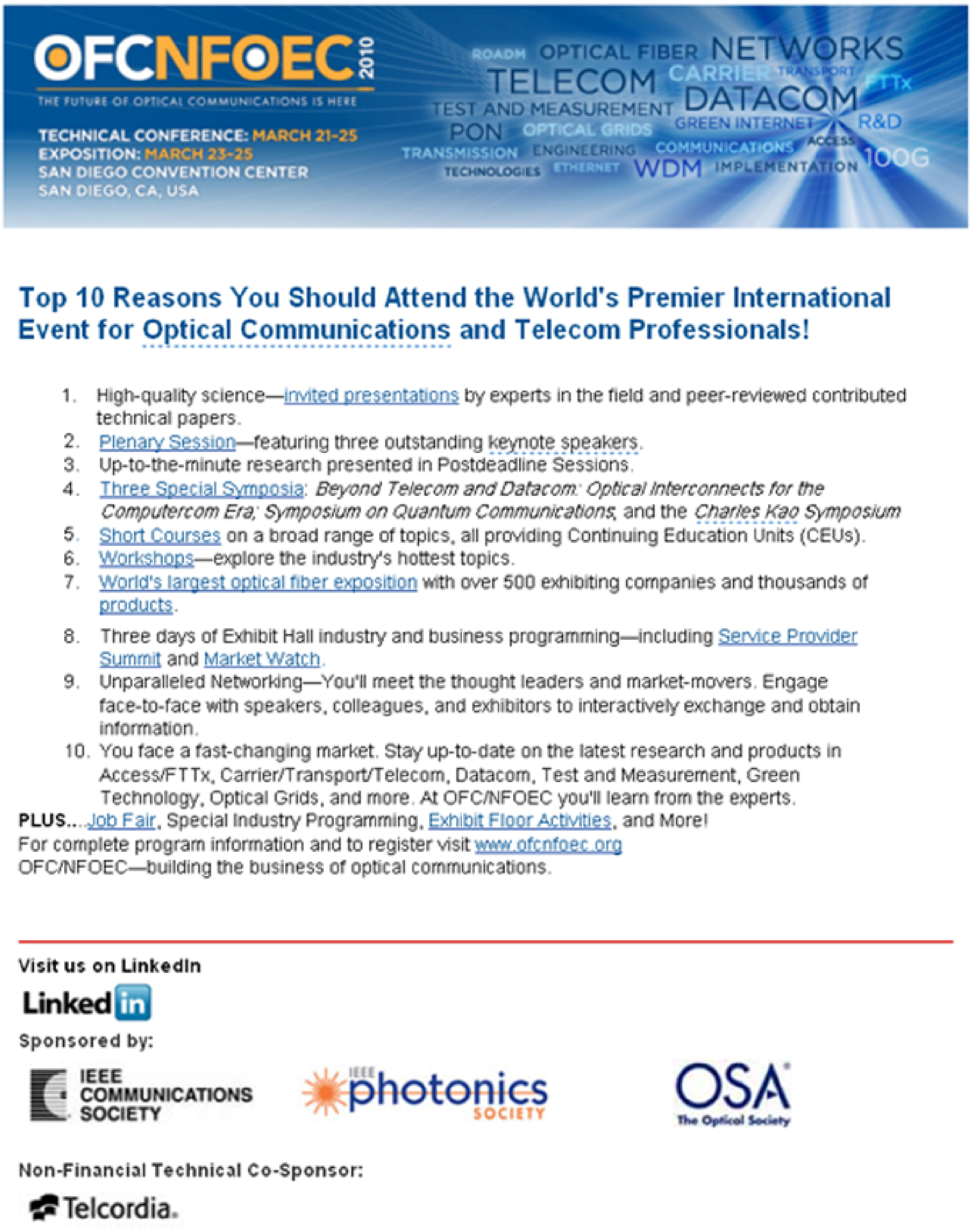
OFCNFOEC 2010
THE FUTURE OF OPTICAL COMMUNICATIONS IS HERE
TECHNICAL CONFERENCE: MARCH 21-25
EXPOSITION: MARCH 23-25
SAN DIEGO CONVENTION CENTER
SAN DIEGO, CA, USA

Top 10 Reasons You Should Attend the World's Premier International Event for Optical Communications and Telecom Professionals!

1. High-quality science—invited presentations by experts in the field and peer-reviewed contributed technical papers.
2. Plenary Session—featuring three outstanding keynote speakers.
3. Up-to-the-minute research presented in Postdeadline Sessions.
4. Three Special Symposia: *Beyond Telecom and Datacom: Optical Interconnects for the Computercom Era; Symposium on Quantum Communications*, and the *Charles Kao Symposium*
5. Short Courses on a broad range of topics, all providing Continuing Education Units (CEUs).
6. Workshops—explore the industry's hottest topics.
7. World's largest optical fiber exposition with over 500 exhibiting companies and thousands of products.
8. Three days of Exhibit Hall industry and business programming—including Service Provider Summit and Market Watch.
9. Unparalleled Networking—You'll meet the thought leaders and market-movers. Engage face-to-face with speakers, colleagues, and exhibitors to interactively exchange and obtain information.
10. You face a fast-changing market. Stay up-to-date on the latest research and products in Access/FTTx, Carrier/Transport/Telecom, Datacom, Test and Measurement, Green Technology, Optical Grids, and more. At OFC/NFOEC you'll learn from the experts.

PLUS... Job Fair, Special Industry Programming, Exhibit Floor Activities, and More!
For complete program information and to register visit www.ofcnfoec.org
OFC/NFOEC—building the business of optical communications.

Visit us on LinkedIn

Sponsored by:

IEEE COMMUNICATIONS SOCIETY
IEEE photonics SOCIETY
OSA The Optical Society

Non-Financial Technical Co-Sponsor:

Telcordia.

THE IRAQI JOURNAL OF
APPLIED PHYSICS LETTERS
EDITORIAL BOARD

COPYRIGHY RELEASE

Iraqi Journal of Applied Physics Letters (IJAPLett)

We, the undersigned, the author/authors of the article titled

………

………

………

………

that is presented to the Iraqi Journal of Applied Physics Letters (IJAPLett) for publication, declare that we have neither taken part or full text from any published work by others, nor presented or published it elsewhere in any other journal. We also declare transferring copyrights and conduct of this article to the Iraqi Journal of Applied Physics Letters (IJAPLett) after accepting it for publication.

The authors will keep the following rights:

1. **Possession of the article such as patent rights.**
2. **Free of charge use of the article or part of it in any future work by the authors such as books and lecture notes without referring to the IJAPLett.**
3. **Republishing the article for any personal purposes of the authors after taking journal permission.**

To be signed by all authors:

Signature:…………………………………………………..date: ………………………………………..
Printed name: ………………………………………………………………………………………………..
Signature:…………………………………………………..date: ………………………………………..
Printed name: ………………………………………………………………………………………………..
Signature:…………………………………………………..date: ………………………………………..
Printed name: ………………………………………………………………………………………………..

Correspondence address:……………………………………………………………………………………
Telephone:………………………Fax:…………………………………..email: …………………………

Note: Please complete and sign this form and mail it to the below address with your manuscript

The Iraqi Journal of Applied Physics Letters
P. O. Box 55259, Baghdad 12001, IRAQ
Email: ijaplett@ijap.org, ijaplett.editor@hotmail.com
Mobile: +964-7702523071

CONTENTS

VOL. 3 , NO. 1 , JANUARY – MARCH 2010